Schmincke, H.-U., Weaver, P.P.E., Firth, J.V., et al., 1995
Proceedings of the Ocean Drilling Program, Initial Reports, Vol. 157

8. SITE 954[1]

Shipboard Scientific Party[2]

HOLE 954A

Date occupied: 4 September 1994

Date departed: 5 September 1994

Time on hole: 1 day, 6 hr, 32 min

Position: 28°26.197′N, 15°31.928′W

Bottom felt (drill-pipe measurement from rig floor, m): 3496.5

Distance between rig floor and sea level (m): 11.30

Water depth (drill-pipe measurement from sea level, m): 3485.2

Total depth (from rig floor, m): 3580.30

Penetration (m): 83.80

Number of cores (including cores having no recovery): 12

Total length of cored section (m): 83.80

Total core recovered (m): 80.46

Core recovery (%): 96

Oldest sediment cored:
Depth (mbsf): 83.80
Nature: lapillistone
Earliest age: Pleistocene

HOLE 954B

Date occupied: 5 September 1994

Date departed: 8 September 1994

Time on hole: 3 days, 00 hr, 17 min

Position: 28° 26.191′N, 15°31.921′W

Bottom felt (drill-pipe measurement from rig floor, m): 3496.5

Distance between rig floor and sea level (m): 11.30

Water depth (drill-pipe measurement from sea level, m): 3485.2

Total depth (from rig floor, m): 3942.50

Penetration (m): 446.00

Number of cores (including cores having no recovery): 39

Total length of cored section (m): 365.80

Total core recovered (m): 165.56

Core recovery (%): 45.3

Oldest sediment cored:
Depth (mbsf): 365.80
Nature: basaltic breccia
Earliest age: middle Miocene

Principal results: Site 954, the second of four sites to be drilled into the volcanic apron of Gran Canaria, is located 34 km northeast of Gran Canaria, 130 km west of Fuerteventura, and 60 km east of Tenerife, at a water depth of 3485 mbsl.

Although no structural or other complications were indicated on the high-resolution pre-site survey data, additional reflection seismic data was acquired on our approach to Site 954 because an investigation of Admiralty Chart 1869 revealed the presence of an underwater cable within a half mile of the proposed location. This short seismic survey repositioned the site approximately 1.3 nmi east of the original prospectus site. The pre-site survey profiles show a sequence, about 0.4 s thick, with an almost parallel layering overlying an acoustic reflector dipping to the north.

The objective of drilling at Site 954 was to study the evolution of Gran Canaria as reflected in the amount, composition, and type of *proximal* volcaniclastic sediments deposited north of the island, close to an area of young volcanism in northern Gran Canaria, and to drill into acoustic basement assumed to represent the flank of the island.

Drilling at Site 954 recovered a 446-m-thick succession of middle Miocene to Holocene sediments, consisting dominantly of fine-grained sediments interbedded with coarser bioclastic and volcaniclastic material. The sequence is interrupted by at least four possibly slump-related hiatuses: at about 80 mbsf in the lower Pleistocene to upper Pliocene (~1 to 1.9 Ma); at ~235 mbsf in the lower Pliocene (~4.4 to 5.3 Ma); at 373 mbsf in the upper Miocene (~8.8 to 9.4 Ma); and between the lowermost sediments of lithologic Unit III and the top of the basal basaltic breccia of lithologic Unit IV (408 mbsf). Preservation and abundance of calcareous nannofossils are generally good throughout the hole. Planktonic foraminifers, in contrast, are poorly preserved below about 280 mbsf except in the basalt breccia where they are well preserved in the lithified matrix.

A preliminary but not continuous magnetostratigraphy consistent with the biostratigraphy was determined to a depth of 408 mbsf (~11 Ma) but not in the underlying basalt breccia.

The sediments were divided into four major units:

Unit I (0–158 mbsf): late Pliocene to Holocene (0–3 Ma). In the upper part of the sequence, sediments are dominantly clayey nannofossil ooze with foraminifers, graded clayey nannofossil mixed sediment, and calcareous sand with lithics. Minor interbeds of crystal lithic sand, pumice sand, and vitric ash layers occur throughout the upper part of Unit I. The remarkable sands rich in neritic biogenic material and coarse volcanic clasts recovered in the upper 100 m are even more coarse grained than similar sands recovered at Site 953. They are interpreted as beach sands redeposited as turbidites, the emplacement of which was possibly related to glacially controlled changes in sea level. The minor thin fallout tephra layers at this site (probably erupted in Tenerife) are also coarser grained than at Site 953, and pumice is more abundant. Recovery was excellent in the upper part of the unit (APC coring) but poor in the lower half, from 80 to 175 m.

Unit II (177–179 mbsf): late Pliocene. A 2-m-thick, dark greenish-gray lapillistone containing abundant mafic volcanic clasts. The lapillistone unit is overlain by a dolomitized siltstone, and dolomitization occurs sporadically throughout the lower part of the underlying unit. The lapillistone resembles lapillistones of roughly similar age in Unit II of Site 953, and it coincides closely in time, mineralogical, and chemical composition with the Roque Nublo volcanic phase on Gran Canaria.

[1] Schmincke, H.-U., Weaver, P.P.E., Firth, J.V., et al., 1995. *Proc. ODP, Init. Repts.*, 157: College Station, TX (Ocean Drilling Program).
[2] Shipboard Scientific Party is given in the list preceding the Table of Contents.

Unit III (180–407 mbsf): early Pliocene to late Miocene (4.3–11 Ma). Recovery was poor again in the upper 90 m, which consist dominantly of gray to brownish-gray, thick nannofossil chalk and clayey nannofossil mixed sedimentary rock with minor crystal lithic sandstone, and siltstone interbeds. Coarse volcaniclastic material not unexpectedly is almost absent in this interval, which approximately coincides with the major hiatus in volcanism on Gran Canaria. The base of the sediments in Unit III is assigned to calcareous nannofossil Zone CN 6/7 and dates from ~9.4–10.8 Ma.

Unit IV (408–446 mbsf): no older than 15–14 Ma. Acoustic basement consists of a thick breccia, of which 38 m was drilled, comprising basalt clasts with minor green hyaloclastite tuffs, lapillistones, and a matrix of calcareous sediments and clay. The breccia age was determined according to foraminifers that were identified in thin section as belonging to Zone M7. Basalt clasts represent both subaerial and shallow submarine eruptions as indicated by rinds of vesicular pillows and are interpreted to represent the emergent stage of the shield volcano. Mineralogical and chemical composition of basalt clasts and volcaniclastic rocks allow us to clearly distinguish the shield and the younger phases and are consistent with the chemical composition of the subaerial shield basalts from Gran Canaria (Schmincke, 1982).

Volcaniclastic rocks representing most of the Fataga and Mogan phases of dominantly explosive volcanism on Gran Canaria (10–14.0 Ma) are completely missing. It is not clear whether the basalt breccia is much thicker than that drilled and whether it rests on entirely submarine rocks or if it represents a slide block that has overridden the Fataga and Mogan sediments.

Extreme pore-water compositions occur immediately above and below the lapillistone of Unit II at 180 mbsf and below 400 mbsf in the boundary interval between nannofossil chalk Unit III and the underlying basaltic breccia Unit IV. Large increases in alkalinity, salinity, sodium, lithium, silica, magnesium, and calcium, and low chlorinity are here associated with CO_2-charged effervescent pore waters. Alkalinities of up to 120 mmol/L are recorded with more than 250 µmol/L Li and 1500 µmol/L Si.These characteristics are tentatively attributed to alteration of glasses and the introduction of CO_2-charged fluids associated with Holocene volcanic activity in northern Gran Canaria. The proximity of the site to an area of young volcanism is also reflected in the high geothermal gradient (52.7°C/km) and the heat flow (52.7 mW/m^2) at average conductivities of 1.0 W/(m·K). Dolomitization is widespread below Core 157-954B-11R.

Seismic and lithostratigraphic correlation between Sites 953 and 954 is good to excellent despite poor recovery in part of the Hole 954B. Significant volcaniclastic material supplied to the site from other islands appears to be restricted to late Pliocene and Pleistocene fallout tephra layers, presumably from Tenerife.

An accumulation rate based on an integrated biostratigraphy and magnetostratigraphy sedimentation rate curve, reasonably constrained above ~370 mbsf, reflects the major contrast between volcanically active phases (Roque Nublo and post-Roque Nublo) and nonvolcanic periods, chiefly the time between approximately 8 and 5 Ma. Accumulation rates are as high as 75 m/m.y. from 0 to 80 mbsf, possibly a combination of high pelagic background sedimentation coupled with periodic influx of thick coarse-grained "beach sands," and relatively high ash and pumice input from Tenerife. Rates fall to ~59 m/m.y. from 80 to 235 mbsf, which includes the phase of Roque Nublo volcanism, and the rates are only 40 m/m.y. during the central part of the volcanic hiatus between 5 and 9 Ma (235–370 mbsf). Accumulation rates were probably much higher during accumulation of the basal breccia flows.

The amount of quartz in the coarse fraction is negligible, as in the sediments of Site 953, contrasting with the high abundance of quartz in the sediments of DSDP Site 397 (Leg 47A). The near absence of quartz and of organic-rich sediments at Site 954 indicates that the basin north of Gran Canaria was largely cut off from turbidity currents and slumps originating at the African continental margin because of the barrier of the older eastern Canary Islands and the high submarine ridge between Gran Canaria and Fuerteventura.

In summary, the geologic evolution of Gran Canaria is well reflected in the sediments cored at Site 954 although not as fully as at Site 953 because of poor recovery between 80 and 270 mbsf and the ~4 m.y. hiatus between the lowermost marly sediments and the basement basalt breccia. The chemical and mineralogical composition of basaltic clasts indicates that the breccia represents the basaltic shield and most likely forms a cover above the true submarine seamount stage of the island. The young volcanic activity on Gran Canaria, which is documented on land by a string of scoria cones and lava flows that are ~3000 yr old (Schmincke, 1982), is dramatically reflected in the high heat flow and in the CO_2-charged pore waters at 180 mbsf and above the basal breccia that most likely reflects the degassing of mafic magma at depth. The extreme compositions of these pore waters suggest strong leaching of the volcaniclastic units by these fluids.

BACKGROUND AND OBJECTIVES

Background

Site 954, the second of four sites to be drilled into the volcanic apron peripheral to Gran Canaria, is located near the southern edge of the northern sedimentary basin just off the steep northern submarine flank of Gran Canaria. Site 954 is 32 km from the northern coast of Gran Canaria and 59 km from the northern tip of Tenerife. Water depth is 3485.2 m.

Objectives

The objectives of drilling at Sites 953 and 954 are similar, with Site 953 representing the more distal and Site 954 the more proximal facies of the northern volcaniclastic apron. The basin sediments north of Gran Canaria are expected to differ significantly from those in the south on account of much higher sedimentation rates and concentration of post-Miocene volcanic activity in the north.

Proximal Facies of the Volcanic Apron of Gran Canaria

We aim to drill into the acoustic basement (submarine flank) beneath the sedimentary cover. We want to compare the volcaniclastic facies on the steeper flank at Site 954 with the distal lower submarine slope facies of the submarine volcanic edifice at Site 953 to better understand volcanic constructive and mass wasting processes of the seamount stage of shield volcanoes. Major mass wasting events are more likely to be found at this than at the other VICAP sites.

Volcanic Sediment Budget

Based on tracing seismic reflectors from the basin to the island, the thickness of the sediment sequence above the island flank is about 30% less, compared to that at Site 953. We want to find out whether this discrepancy results from (1) a general thinning of the entire sequence or of certain intervals, (2) successive onlapping so that some intervals at Site 953 were not deposited, or (3) removal of parts of the section by slumping. This type of information is crucial for calculating sediment budgets for the submarine growth, subaerial evolution, and unroofing of Gran Canaria. They are also fundamental to the question of how well volcanic and nonvolcanic periods on an island are reflected in the amount, composition and type of volcaniclastic sediment laid down per time unit in the proximal basin north of the island.

Diagenesis

Temperature gradients in this most proximal site are likely appreciably higher than in any of the other proposed drill sites into the apron especially since the late Pliocene to Holocene volcanic centers are all located in the northern half of the island. Volcanic glass might therefore be less stable in these proximal sediments, cementation more advanced and the variety of secondary minerals higher than at any other drill site into the apron.

Ash Layer Depositional Fans and Paleowind Directions

Being at roughly half the distance between Site 953 and Tenerife we expect more and thicker ash layers from the late Pliocene/Pleistocene explosive phases of Teide Volcano than at Site 953. Thickness and grain size are important in reconstructing the depositional fans and therefore paleowind directions during the Pleistocene.

UNDERWAY GEOPHYSICS

On our approach to Site 954 a 9.5-km-long reflection seismic profile was acquired starting at 28°28.9′N, 15°30.8′W and ending at 28°24.1′N, 15°32.8′W. An 80 in.^{3} water gun was used as a seismic source and the signals were recorded on a single-channel streamer and displayed on line-scan recorders for immediate inspection. The shot interval was 10 s corresponding to a distance of ~30 m. Data were stored digitally on 8 mm tape and subsequently processed by shipboard SIOSEIS software. The processing sequence was as follows: bandpass filter (60–120 Hz), automatic gain control (500 ms window), finite difference migration, bandpass filter (60–120 Hz), trace mix (weights 1 2 1), mute, and display. The processed profile is shown in Figure 1 and an interpretation is shown as a line drawing in Figure 2.

The penetration increases from ~200 ms below the seafloor in the southern side of the profile to ~720 ms in the northern side. The deepest reflector in general has a high amplitude and a good continuity. This northward dipping reflector defines the acoustic basement except in the southernmost part of the profile where a nearly horizontal, high-amplitude reflector appears below the dipping reflector at ~350 ms below the seafloor. A step-like depth change with a height of ~160 ms, facing northward, cuts the acoustic basement in the middle of the profile. North of this step the acoustic basement appears as a slightly undulating surface with a gentle northward dip. South of the step the acoustic basement has an average dip of 2° to the north. The basement reflector appears here to be composed of a series of stacked mounds where the younger mounds tend to step successively backward in an upslope direction. The horizontal reflector mentioned above forms the floor of the uppermost mound.

The sequence that covers the acoustic basement is characterized by subparallel reflectors that onlap the basement. Two seismic units, A and B, can be discerned. The upper unit (A) has a nearly constant thickness (100–120 ms) and is bounded on top and base by pairs of high-amplitude reflectors. Internal reflectors have relatively high amplitudes and generally short periods. The reflectors are mostly concordant and parallel to the seafloor, but in the central part of the profile, in the vicinity of Site 954, the internal reflector pattern as well as the seafloor topography are more complex. The complex structures may image debris flows.

Unit B is relatively transparent, but a few reflectors can easily be traced through the profile to the point of onlap at the basement. There is a conspicuous change toward higher amplitudes on the northern side of the step in the basement. This change coincides with a minor reduction in dip of the reflectors. A small basin is located vertically above the step in the basement approximately in the middle of Unit B. Immediately beneath the basin a relatively strong reflector appears to be broken, possibly indicating a fault downthrown to the north.

Depth estimates for the main reflectors indicated in Figure 2 at Site 954 were obtained by applying the two-way traveltime vs. depth relationship established at Site 953 (see Fig. 69, "Site 953" chapter, this volume).

OPERATIONS

Site 953 to Site 954 Transit

The ship averaged 11.7 kt over the 21 nmi to the survey point. The initial plan was to transit to the location and drop a beacon on GPS coordinates. However, an investigation of Admiralty Chart 1869 revealed the presence of an underwater cable within 0.5 mi of the proposed location. This necessitated a short seismic survey that repositioned the site approximately 1.3 nmi east of the original prospectus site. The beacon was deployed at 1341, local time, 4 September.

Hole 954A (VICAP-2A)

An APC/XCB BHA was made up. Core 157-954A-1H established the mud line depth at 3485.2 mbsl. APC coring advanced to 79.2 m (Table 1), which was considered APC refusal when Core 157-954A-11H only partially stroked. The APC system recovered 100.9% of the interval cored. The cores were oriented starting with Core 157-954A-4H. Heat-flow measurements were conducted on Cores 157-954A-5H and 157-954A-8H. XCB coring began at 79.2 mbsf but was abandoned when Cores 157-954A-11X and 157-954A-12X recovered coarse basaltic breccia with a low ROP of 4 m/hr. In addition, the PDC cutting structure was not well matched to the very coarse gravel. The bit was tripped to the surface to change to the RCB system. At 2013, 5 September, the bit cleared the rotary table, ending Hole 954A. The vessel was offset 20 m south.

Hole 954B

An RCB BHA was made up and Hole 954B was spudded and drilled to 80.2 mbsf. The wash barrel was retrieved and the first rotary core barrel was dropped. RCB coring advanced quickly through what turned out to be a shallow zone (~2 m thick) of basalt breccia that had thwarted the XCB. For the next 100 m recovery was very low because the formation was very soft. Recovery improved with depth as the formation became more indurated. Total penetration was 446.0 mbsf (cored interval of 365.8 m) with 45.5% recovery.

At 1430, 8 September, coring operations were terminated and the hole was swept with a 25 bbl sepiolite flush. The pipe began to be pulled up for logging. At 1522, 8 September, the bit had reached 379 mbsf and was being pulled up with 25,000 lb overpull when a sudden jolt was felt. The driller noticed that the string weight had dropped by 67,000 lb. With the obvious loss of a significant amount of hardware, logging was canceled, and the pipe was pulled out of the hole. At 2013, 8 September, the bottom of the drill string cleared the rig floor. Inspection of the recovered drill pipe indicated that a pin failure at the last engaged thread on a 5 in. tool joint had resulted in the loss of the total BHA, including drilling jars, and 46 joints of 5 in. drill pipe. Initial analysis suggests fatigue failure. The remaining tool joint will be sent to shore for further analysis.

After the drill pipe was pulled and the hydrophones and thrusters were secured, the vessel departed for prospectus site VICAP-4 (Site 955) at 2030, 8 September.

LITHOSTRATIGRAPHY

The sedimentary succession recovered at Site 954 is 446 m thick and consists of abundant fine-grained sediments interbedded with coarser bioclastic and volcaniclastic material (Fig. 3). The age of the sequence ranges from Pleistocene to middle Miocene. In the upper part of the sequence, the major lithologies include clayey nannofossil ooze with foraminifers, graded clayey nannofossil mixed sediment, and calcareous sand with lithics. Minor interbeds of crystal lithic

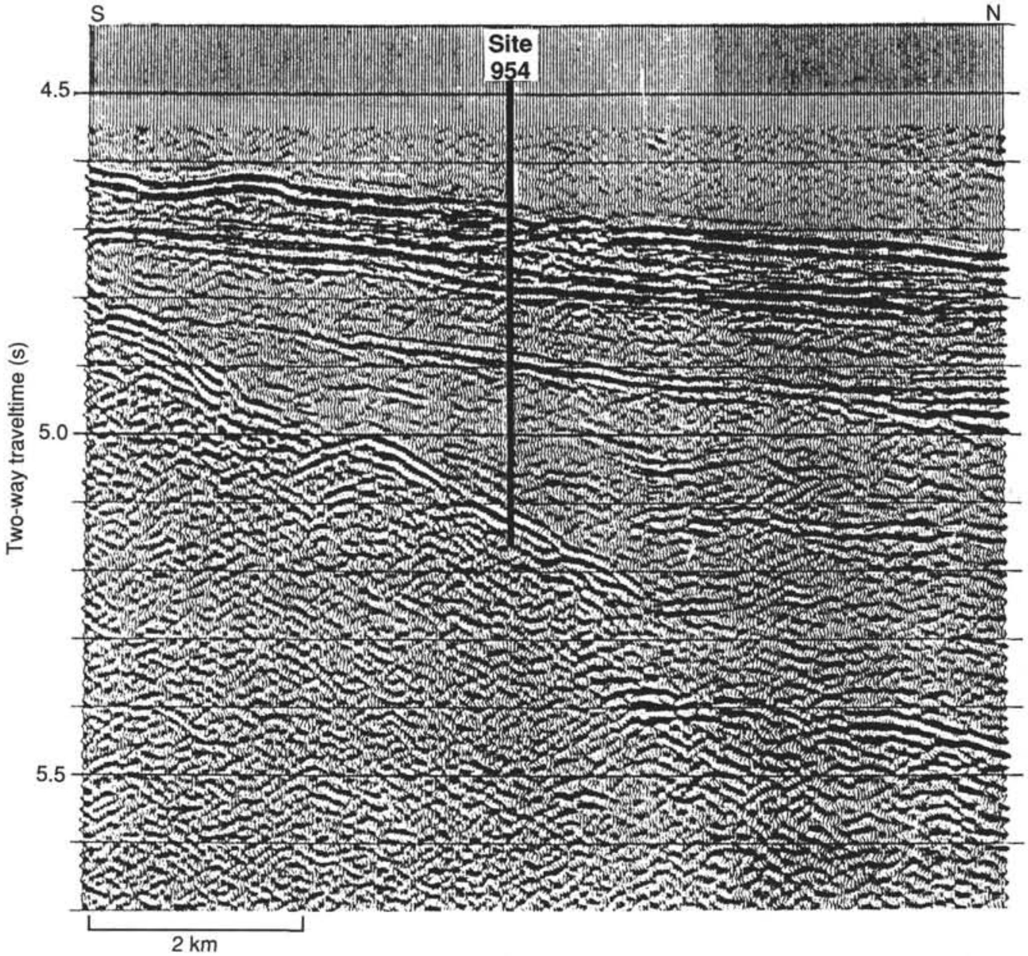

Figure 1. Processed seismic profile acquired during approach to Site 954.

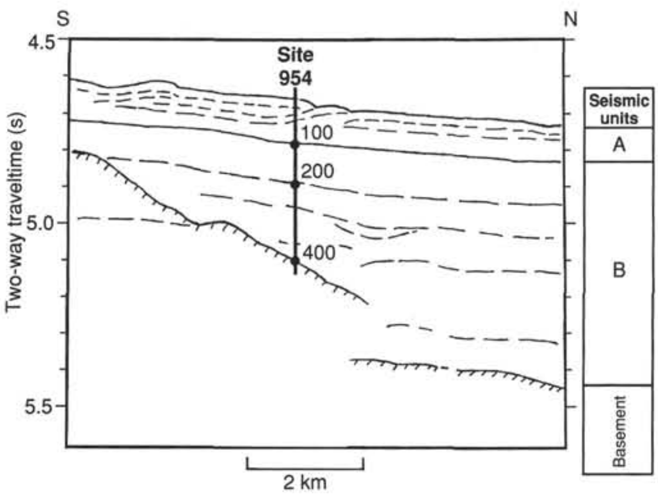

Figure 2. Interpretation of the seismic profile. Estimated depth (mbsf) to the main reflectors is given at Site 954.

sand, pumice sand, and vitric ash layers occur throughout the upper part of the sedimentary sequence. The middle part of the sequence is characterized by thick nannofossil chalk and clayey nannofossil mixed sedimentary rock with minor lapillistone, crystal lithic sandstone, and siltstone interbeds. A thick basaltic breccia occurs at the base of the sequence below acoustic basement. The proportions and lithology of volcaniclastic material, principally from Gran Canaria has been used as criteria for subdividing the sequence at Site 954 into four units (I–IV) (Fig. 4).

Calcium carbonate data show a similar trend to that noted at Site 954. Carbonate concentrations in the pelagic sediments mostly range between 50% and 80% from 0 to 200 mbsf (Units I and II; Fig. 5). In the upper part of Unit III (200–300 mbsf) calcium carbonate content ranges between 60% and 85% but decreases and becomes more variable (35% and 75%) in the lower part of the unit between 300 and 410 mbsf (Fig. 5). Calcium carbonate content in the turbidite muds follows the trend of the pelagic sediments but with concentrations generally 10% to 30% less (Fig. 5).

Unit I

Interval: Sections 157-954A-1H-1 to 157-953B-10R
Depth: 0–177 mbsf
Age: Pleistocene to late Pliocene

Table 1. Coring summary, Holes 954A and 954B.

Core	Date (August 1994)	Time (UTC)	Sub-bottom (m) Top	Sub-bottom (m) Bottom	Cored (m)	Recovered (m)	Recovery (%)	Section	Length (m)	Depth (mbsf) Top	Depth (mbsf) Bottom	Samples
157-954A-												
1H	4	2330	0.0	1.0	1.0	1.07	107.0					
								1	0.86	0.00	0.86	HS 81-86
								CC	0.21	0.86	1.07	
2H	5	0025	1.0	10.5	9.5	8.84	93.0					
								1	1.50	1.00	2.50	
								2	1.50	2.50	4.00	
								3	1.50	4.00	5.50	
								4	1.50	5.50	7.00	
								5	1.50	7.00	8.50	HS 0-5
								6	1.16	8.50	9.66	
								CC	0.18	9.66	9.84	
3H	5	0110	10.5	20.0	9.5	9.24	97.2					
								1	1.50	10.50	12.00	IW 145-150
								2	1.50	12.00	13.50	HS 0-5
								3	1.50	13.50	15.00	
								4	1.50	15.00	16.50	
								5	1.50	16.50	18.00	
								6	1.50	18.00	19.50	
								CC	0.24	19.50	19.74	
4H	5	0205	20.0	29.5	9.5	9.52	100.0					
								1	1.50	20.00	21.50	
								2	1.50	21.50	23.00	
								3	1.50	23.00	24.50	
								4	1.50	24.50	26.00	IW 145-150
								5	1.50	26.00	27.50	HS 0-5
								6	1.50	27.50	29.00	
								7	0.27	29.00	29.27	
								CC	0.25	29.27	29.52	
5H	5	0320	29.5	39.0	9.5	9.61	101.0					
								1	1.50	29.50	31.00	
								2	1.50	31.00	32.50	
								3	1.50	32.50	34.00	IW 145-150
								4	1.50	34.00	35.50	HS 0-5
								5	1.50	35.50	37.00	
								6	1.50	37.00	38.50	
								7	0.44	38.50	38.94	
								CC	0.17	38.94	39.11	
6H	5	0410	39.0	48.5	9.5	9.46	99.6					
								1	1.50	39.00	40.50	
								2	1.50	40.50	42.00	
								3	1.50	42.00	43.50	
								4	1.50	43.50	45.00	
								5	1.50	45.00	46.50	IW 145-150
								6	1.50	46.50	48.00	HS 0-5
								7	0.23	48.00	48.23	
								CC	0.23	48.23	48.46	
7H	5	0505	48.5	58.0	9.5	9.59	101.0					
								1	1.50	48.50	50.00	
								2	1.50	50.00	51.50	
								3	1.50	51.50	53.00	IW 145-150
								4	1.50	53.00	54.50	HS 0-5
								5	1.50	54.50	56.00	
								6	1.50	56.00	57.50	
								7	0.56	57.50	58.06	
								CC	0.03	58.06	58.09	
8H	5	0620	58.0	67.5	9.5	10.11	106.4					
								1	1.50	58.00	59.50	
								2	1.50	59.50	61.00	
								3	1.50	61.00	62.50	
								4	1.50	62.50	64.00	
								5	1.50	64.00	65.50	IW 145-150
								6	1.50	65.50	67.00	HS 0-5
								7	0.64	67.00	67.64	
								CC	0.47	67.64	68.11	
9H	5	0720	67.5	77.0	9.5	10.18	107.1					
								1	1.50	67.50	69.00	
								2	1.50	69.00	70.50	
								3	1.50	70.50	72.00	
								4	1.50	72.00	73.50	
								5	1.50	73.50	75.00	IW 145-150
								6	1.50	75.00	76.50	HS 0-5
								7	0.90	76.50	77.40	
								CC	0.28	77.40	77.68	
10H	5	0810	77.0	79.2	2.2	2.25	102.0					
								1	1.50	77.00	78.50	IW 145-150
								2	0.72	78.50	79.22	HS 0-5
								CC	0.03	79.22	79.25	
11X	5	1030	79.2	82.8	3.6	0.38	10.5					
								CC	0.38	79.20	79.58	
12X	5	1125	82.8	83.8	1.0	0.15	15.0					
								CC	0.15	82.80	82.95	
Coring Totals					83.8	80.4	95.90					
157-954B-												
1R	6	0935	80.2	90.4	10.2	1.15	11.3					
								1	1.32	80.20	81.52	

Table 1 (continued).

Core	Date (August 1994)	Time (UTC)	Sub-bottom (m) Top	Sub-bottom (m) Bottom	Cored (m)	Recovered (m)	Recovery (%)	Section	Length (m)	Depth (mbsf) Top	Depth (mbsf) Bottom	Samples
2R	6	1020	90.4	100.1	9.7	0.00	0.0					
3R	6	1110	100.1	109.7	9.6	0.01	0.1					
								CC	0.01	100.10	100.11	
4R	6	1200	109.7	119.3	9.6	3.19	33.2					
								1	1.50	109.70	111.20	IW 140-150
								2	1.48	111.20	112.68	HS 0-5
								CC	0.21	112.68	112.89	
5R	6	1255	119.3	129.0	9.7	6.45	66.5					
								1	1.50	119.30	120.80	
								2	1.50	120.80	122.30	
								3	1.50	122.30	123.80	
								4	1.50	123.80	125.30	HS 0-5
								5	0.31	125.30	125.61	
								CC	0.14	125.61	125.75	
6R	6	1355	129.0	138.6	9.6	6.23	64.9					
								1	1.50	129.00	130.50	
								2	1.50	130.50	132.00	
								3	1.50	132.00	133.50	IW 140-150
								4	1.50	133.50	135.00	HS 0-5
								CC	0.23	135.00	135.23	
7R	6	1450	138.6	148.2	9.6	5.80	60.4					
								1	1.50	138.60	140.10	
								2	1.50	140.10	141.60	
								3	1.50	141.60	143.10	
								4	1.09	143.10	144.19	HS 0-5
								CC	0.21	144.19	144.40	
8R	6	1555	148.2	157.9	9.7	2.92	30.1					
								1	1.30	148.20	149.50	IW 120-130
								2	1.41	149.50	150.91	HS 0-5
								CC	0.21	150.91	151.12	
9R	6	1705	157.9	167.6	9.7	0.10	1.0					
								1	0.10	157.90	158.00	
10R	6	1815	167.6	177.2	9.6	0.00	0.0					
11R	6	1945	177.2	186.9	9.7	3.08	31.7					
								1	1.37	177.20	178.57	
								2	1.34	178.57	179.91	IW 97-107
								3	0.36	179.91	180.27	HS 0-5
								CC	0.27	180.27	180.54	
12R	6	2055	186.9	196.5	9.6	3.51	36.5					
								1	1.50	186.90	188.40	
								2	1.50	188.40	189.90	HS 0-5
								3	0.28	189.90	190.18	
								CC	0.23	190.18	190.41	
13R	6	2155	196.5	206.2	9.7	2.95	30.4					
								1	1.50	196.50	198.00	IW 140-150
								2	1.23	198.00	199.23	HS 0-5
								CC	0.22	199.23	199.45	
14R	6	2255	206.2	215.7	9.5	0.21	2.2					
									CC	0.21	206.20	206.41
15R	6	2350	215.7	225.2	9.5	2.19	23.0					
								1	1.15	215.70	216.85	IW 105-115
								2	1.01	216.85	217.86	HS 0-5
								CC	0.03	217.86	217.89	
16R	7	0045	225.2	234.8	9.6	2.22	23.1					
								1	1.50	225.20	226.70	
								2	0.54	226.70	227.24	HS 0-5
								CC	0.18	227.24	227.42	
17R	7	0140	234.8	244.4	9.6	1.10	11.4					
								1	0.90	234.80	235.70	hs 0-5
								CC	0.20	235.70	235.90	
18R	7	0245	244.4	254.1	9.7	3.24	33.4					
								1	1.50	244.40	245.90	IW 140-150
								2	1.50	245.90	247.40	HS 0-5
								CC	0.24	247.40	247.64	
19R	7	0400	254.1	263.7	9.6	1.50	15.6					
								1	1.28	254.10	255.38	HS 0-5
								CC	0.22	255.38	255.60	
20R	7	0520	263.7	273.3	9.6	3.57	37.2					
								1	1.50	263.70	265.20	
								2	1.50	265.20	266.70	HS 0-5
								3	0.37	266.70	267.07	
								CC				
20R	7	0520	263.7	273.3	9.6	3.57	37.2					
								1	1.50	263.70	265.20	
								2	1.50	265.20	266.70	HS 0-5
								3	0.37	266.70	267.07	
								CC	0.22	267.07	267.29	
21R	7	0620	273.3	282.8	9.5	8.85	93.1					
								1	1.50	273.30	274.80	
								2	1.50	274.80	276.30	
								3	1.50	276.30	277.80	
								4	1.50	277.80	279.30	
								5	1.50	279.30	280.80	IW 141-150
								6	1.16	280.80	281.96	HS 0-5
								CC	0.19	281.96	282.15	
22R	7	0720	282.8	292.4	9.6	6.87	71.5					
								1	1.50	282.80	284.30	
								2	1.50	284.30	285.80	

Table 1 (continued).

Core	Date (August 1994)	Time (UTC)	Sub-bottom (m) Top	Sub-bottom (m) Bottom	Cored (m)	Recovered (m)	Recovery (%)	Section	Length (m)	Depth (mbsf) Top	Depth (mbsf) Bottom	Samples
								3	1.50	285.80	287.30	
								4	1.50	287.30	288.80	HS 0-5
								5	0.67	288.80	289.47	
								CC	0.20	289.47	289.67	
23R	7	0820	292.4	302.0	9.6	8.61	89.7					
								1	1.50	292.40	293.90	
								2	1.50	293.90	295.40	
								3	1.50	295.40	296.90	
								4	1.50	296.90	298.40	
								5	1.50	298.40	299.90	HS 0-5
								6	0.95	299.90	300.85	
								CC	0.16	300.85	301.01	
24R	7	0915	302.0	311.7	9.7	3.01	31.0					
								1	1.48	302.00	303.48	IW 133-148
								2	1.50	303.48	304.98	HS 0-5
								CC	0.03	304.98	305.01	
25R	7	1015	311.7	321.4	9.7	1.79	18.4					
								1	1.50	311.70	313.20	
								2	0.26	313.20	313.46	HS 0-5
								CC	0.03	313.46	313.49	
26R	7	1105	321.4	331.1	9.7	6.40	66.0					
								1	1.50	321.40	322.90	
								2	1.50	322.90	324.40	
								3	1.50	324.40	325.90	
								4	1.50	325.90	327.40	HS 0-5
								5	0.40	327.40	327.80	
27R	7	1205	331.1	340.7	9.6	8.45	88.0					
								1	1.50	331.10	332.60	
								2	1.50	332.60	334.10	
								3	1.50	334.10	335.60	IW 140-150
								4	1.50	335.60	337.10	HS 0-5
								5	1.50	337.10	338.60	
								6	0.95	338.60	339.55	
28R	7	1305	340.7	350.4	9.7	4.04	41.6					
								1	1.45	340.70	342.15	
								2	1.39	342.15	343.54	HS 0-5
								3	1.20	343.54	344.74	
29R	7	1430	350.4	359.9	9.5	5.72	60.2					
								1	1.35	350.40	351.75	
								2	1.35	351.75	353.10	
								3	1.29	353.10	354.39	
								4	1.24	354.39	355.63	HS 0-5
								5	0.49	355.63	356.12	
30R	7	1530	359.9	369.4	9.5	9.32	98.1					
								1	1.41	359.90	361.31	
								2	1.01	361.31	362.32	
								3	1.46	362.32	363.78	
								4	1.46	363.78	365.24	
								5	1.41	365.24	366.65	IW 131-141
								6	1.37	366.65	368.02	hs 0-5
								7	1.20	368.02	369.22	
31R	7	1630	369.4	378.9	9.5	8.84	93.0					
								1	1.45	369.40	370.85	
								2	1.45	370.85	372.30	
								3	1.48	372.30	373.78	
								4	1.46	373.78	375.24	
								5	1.40	375.24	376.64	IW 130-140
								6	1.35	376.64	377.99	HS 0-5
								7	0.25	377.99	378.24	
32R	7	1745	378.9	388.5	9.6	9.87	103.0					
								1	1.50	378.90	380.40	
								2	1.31	380.40	381.71	
								3	1.50	381.71	383.21	
								4	1.46	383.21	384.67	IW 136-146/HS 141-146
								5	1.50	384.67	386.17	
								6	1.31	386.17	387.48	
								7	1.04	387.48	388.52	
33R	7	1850	388.5	398.1	9.6	9.69	101.0					
								1	1.50	388.50	390.00	
								2	1.50	390.00	391.50	
								3	1.50	391.50	393.00	
								4	1.50	393.00	394.50	IW 140-150
								5	1.50	394.50	396.00	
								6	1.50	396.00	397.50	
								7	0.51	397.50	398.01	
34R	7	2045	398.1	407.8	9.7	8.67	89.4					
								1	1.50	398.10	399.60	
								2	1.50	399.60	401.10	
								3	1.50	401.10	402.60	
								4	1.50	402.60	404.10	IW 140-150
								5	1.50	404.10	405.60	HS 0-5
								6	0.78	405.60	406.38	
								CC	0.39	406.38	406.77	
35R	8	2355	407.8	417.3	9.5	2.77	29.1					
								1	1.50		409.30	
								2	1.47	407.80	410.77	
								3	0.48	409.30	411.25	
36R	8	0315	417.3	426.8	9.5	3.15	33.1			410.77		
								1	1.43		418.73	
								2	1.46	417.30	420.19	

Table 1 (continued).

Core	Date (August 1994)	Time (UTC)	Sub-bottom (m) Top	Sub-bottom (m) Bottom	Cored (m)	Recovered (m)	Recovery (%)	Section	Length (m)	Depth (mbsf) Top	Depth (mbsf) Bottom	Samples
								3	1.08	418.73	421.27	
37R	8	0815	426.8	436.4	9.6	1.90	19.8			420.19		
								1	1.50		428.30	
								2	0.92	426.80	429.22	
38R	8	1125	436.4	441.2	4.8	4.90	102.0			428.30		
								1	1.46		437.86	
								2	1.37	436.40	439.23	
								3	1.44	437.86	440.67	
								4	1.23	439.23	441.90	
39R	8	1400	441.2	446.0	4.8	3.29	68.5			440.67		
								1	1.41		442.61	
								2	1.42	441.20	444.03	
								3	0.74	442.61	444.77	
										444.03		
Coring totals					365.8	165.6	45.30					

Notes: Hole 954A located at 28°26.197′N, 15°31.928′W. Water depth from sea surface = 3485.2 m. Hole 954B located at 28°26.191′N, 15°31.921′W. Water depth from sea surface = 3485.2 m. HS = headspace samples; IW = interstitial water samples.

Unit I is 177 m thick and consists predominantly of gray to pale white nannofossil ooze with foraminifers and massive bioclastic sands with interbeds of crystal lithic sands, vitric ash (thinly laminated), and lapillistone. The clayey nannofossil ooze occurs as thick structureless or slightly to moderately bioturbated beds and is interpreted as pelagic sediment. Clayey nannofossil mixed sediments are often interbedded with nannofossil oozes and typically grade downward into parallel-laminated, silty or sandy bases (Fig. 6).

Coarse-grained bioclastic foraminiferal sands occur as thick to very thick bedded deposits that are poorly sorted and sometimes normally graded. They contain abundant shallow-water shell debris, planktonic and benthic foraminifers, and minor volcaniclastic grains, such as basalt and phonolite rock fragments, pumice, glass shards, and crystals. These deposits are similar to but thicker and coarser-grained than coarse-grained calcareous deposits that occur in Unit I of Site 953.

Coarse-grained volcaniclastic material also forms discrete deposits within Unit I. A very thick bedded structureless deposit of coarse crystal-lithic sand in Core 157-954A-7H is dark gray to black and contains a small amount of calcareous material. Lapillistones are another type of coarse volcaniclastic deposit, one of which occurs in Core 157-954A-11X and is made up of angular to subrounded volcanic clasts up to 6 cm in diameter, composed mainly of vesicular basalt clasts (Fig. 7). More commonly, volcaniclastic sand occurs as thin to medium bedded deposits with variable amounts of bioclastic material, including foraminifers and shell fragments up to 1 cm long. Many of these units consist of fining-upward sequences with sharp bases and bioturbated clay-rich tops.

Vitric-rich deposits principally occur as two types within Unit I. Most common are thinly laminated to thin bedded volcanic ash layers interpreted as fall deposits (Fig. 8). Each bed is defined by a relatively sharp base and bioturbated top. They are primarily composed of clear glass shards with minor amounts of crystals and lithics, but are more common and thicker than similar vitric ash deposits in Unit I of Site 953.

A second less common variety of vitric-rich deposit is coarser grained and thicker. These typically contain pumice of coarse ash to lapilli-size. An example can be found in Section 157-954B-4R-2 where a pumice sand with rounded pumice fragments at the base grades upward into a fine-grained vitric tuff.

The base of Unit I is marked by the occurrence of a dolomitic siltstone. Core recovery of this lithology was poor, but the interval recovered consists of brown, massive and very strongly dolomitized siltstone.

Unit II

Interval: Sections 157-954B-11R-1 to 157-954B-11R-2
Depth: 177–179 mbsf
Age: late Pliocene

Unit II is 2 m thick and consists of dark greenish-gray lapillistone. It is distinguished from Unit I by the coarse grain size and abundance of mafic volcanic clasts (Fig. 9).

The lapillistone is matrix-supported, poorly sorted, polymict, and normally graded. It contains angular to subangular clasts of phonolite, pyroxene-phyric basalt and minor pumice. Altered feldspars occur in the matrix. The base of the lapillistone may be reversely graded, but coring disturbance precludes a precise assessment of this feature.

The lapillistone unit is overlain by a fine-grained siltstone with a high proportion of dolomite. The light gray nannofossil chalk underneath the lapillistone contains abundant dark crystals and lithics dispersed throughout and is moderately bioturbated.

Although Unit II is here defined as a 2 m interval with excellent recovery, the actual boundaries of the time interval assigned to Unit II in Sites 953, 955, and 956 are likely to extend both above and below the 2 m of lapillistone at Site 954. The time interval represented by "Unit II" at the other VICAP sites (953, 955, and 956) may include the younger cores (no recovery, but possibly coarse-grained volcaniclastic sediments). Similarly, the lower boundary may include the older cores, 157-954B-12R, 13R, and 14R, which show poor or no recovery. A different approach to unit definition was taken at Site 956 where Unit II includes two core intervals at its base with no recovery.

Unit III

Interval: Sections 157-954B-11R-2 to 157-954B-35R-1
Depth: 179–408 mbsf
Age: early Pliocene to late Miocene

Unit III is 226 m thick and the dominant lithology is gray nannofossil chalk interbedded with minor clayey nannofossil mixed sedimentary rock and crystal-lithic siltstones and sandstones. It is distinguished from Unit II in having a greater proportion of fine-grained calcareous sediment and more common slumped sediments (Fig. 4).

Nannofossil chalk occurs as medium to thickly bedded units, which are moderately to heavily bioturbated and may contain silty and clayey interbeds. Some chalk beds contain fine-grained lithic

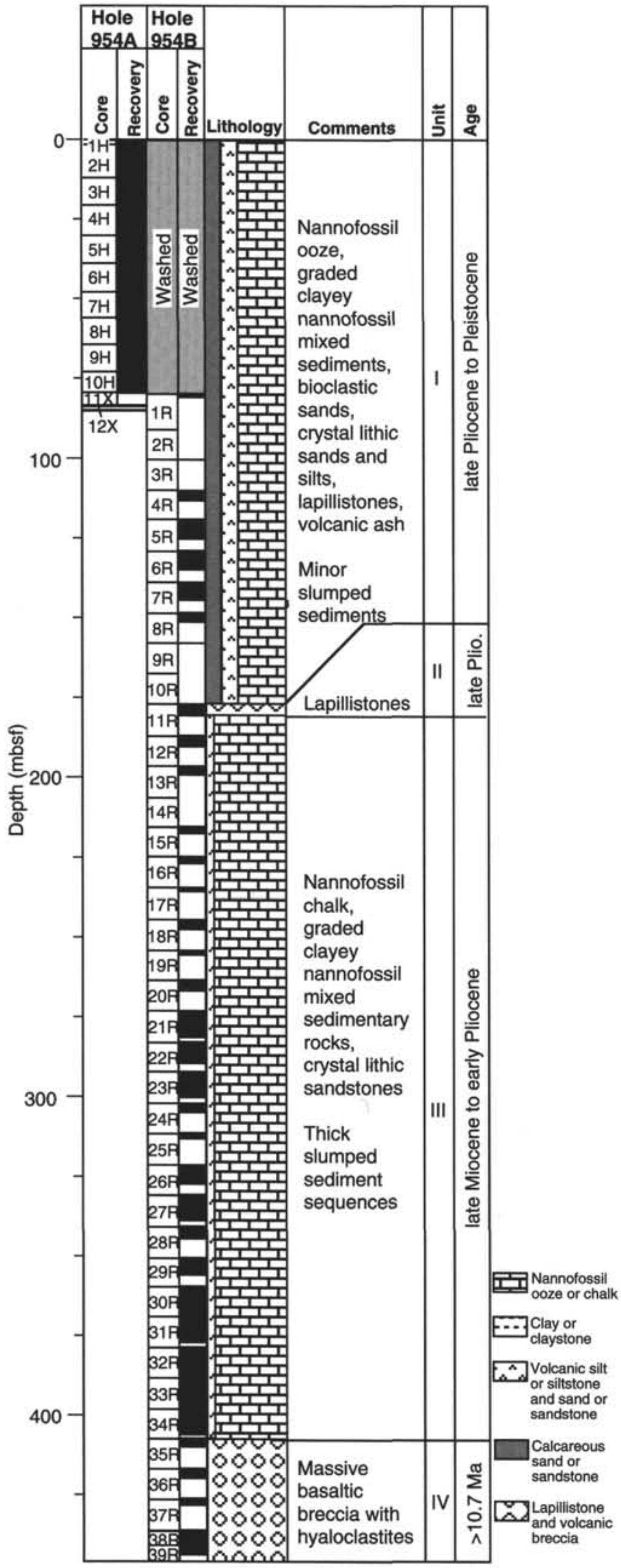

Figure 3. Lithologic summary for Holes 954A and 954B showing the main lithologic units identified with age and a generalized graphic lithology.

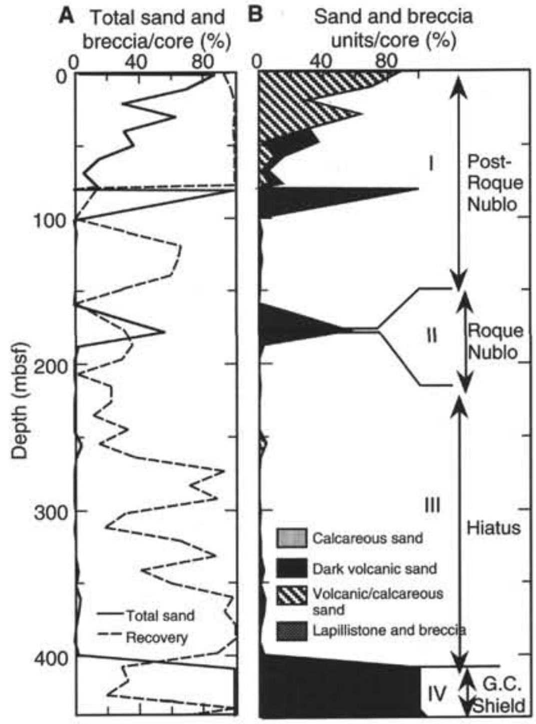

Figure 4. Variation in (**A**) the percentage of coarse (greater than sand size) volcaniclastic layers per core and (**B**) the percentage of different types of sand and breccia layers per core as a function of depth below seafloor. G.C. = Grand Canaria.

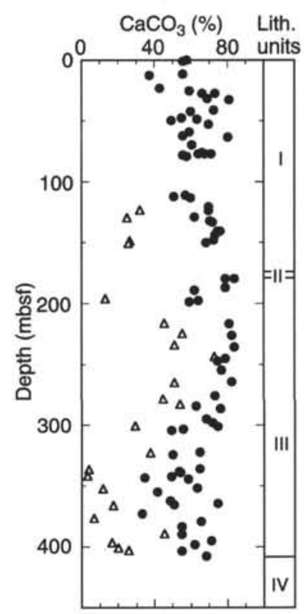

Figure 5. Variation in the calcium carbonate content of pelagic sediment (filled circles) and turbidite muds (open triangles) as a function of depth below seafloor.

particles (basalt) and crystals (amphibole, biotite) that are dispersed throughout (Fig. 10). This clastic material could have been incorporated and mixed into the chalk by either bioturbation, slumping, or wind transported dust.

Clayey nannofossil mixed sedimentary rock occurs as minor interbeds within the nannofossil chalk. Planar lamination often gives a

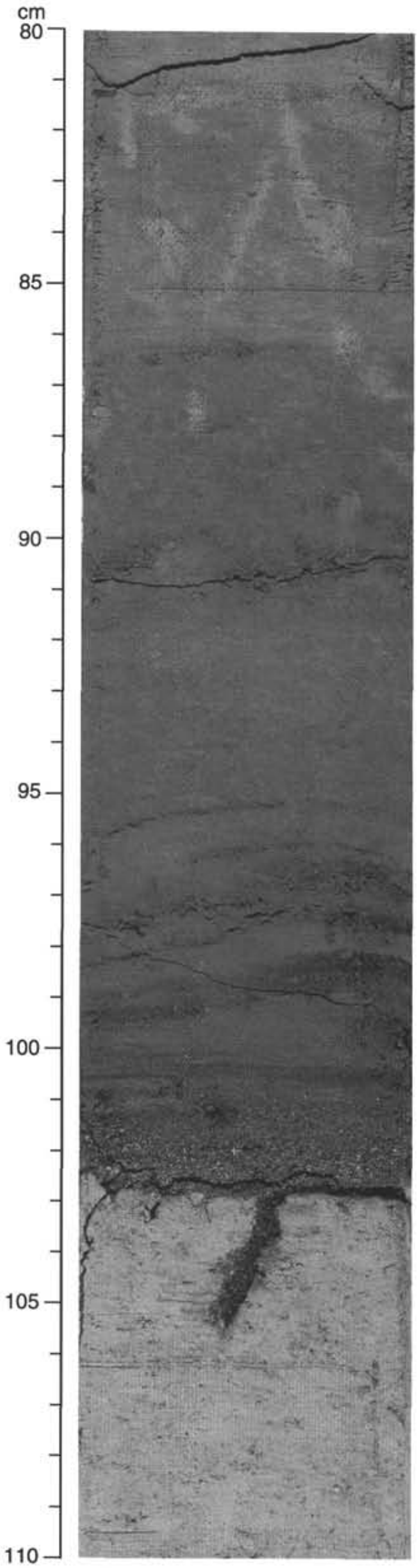

Figure 6. Sandy base of a clayey nannofossil mixed sediment. Note normal grading and parallel lamination underlined by silty laminae. Interval 157-954A-9H-1, 80–110 cm.

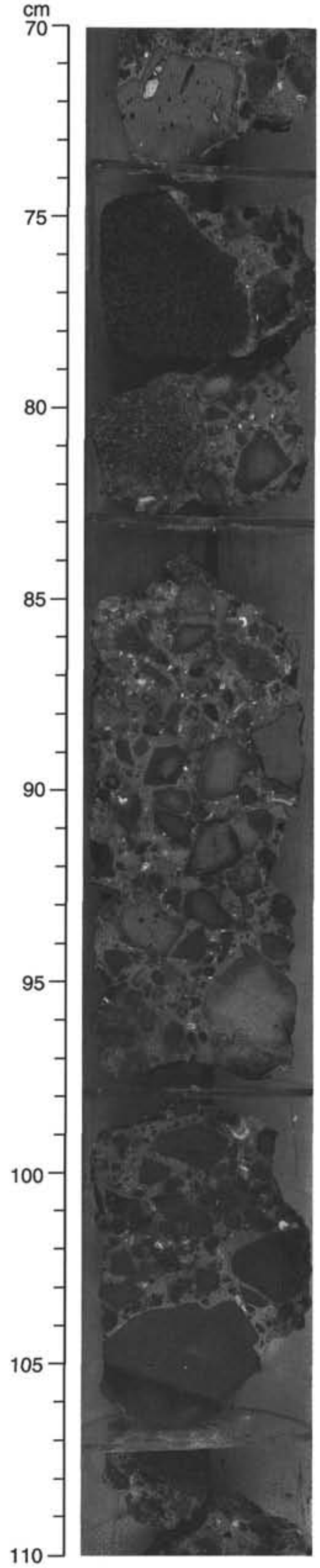

Figure 7. Poorly sorted lapillistone interval within Unit I. Interval 157-954B-1R-1, 70–110 cm.

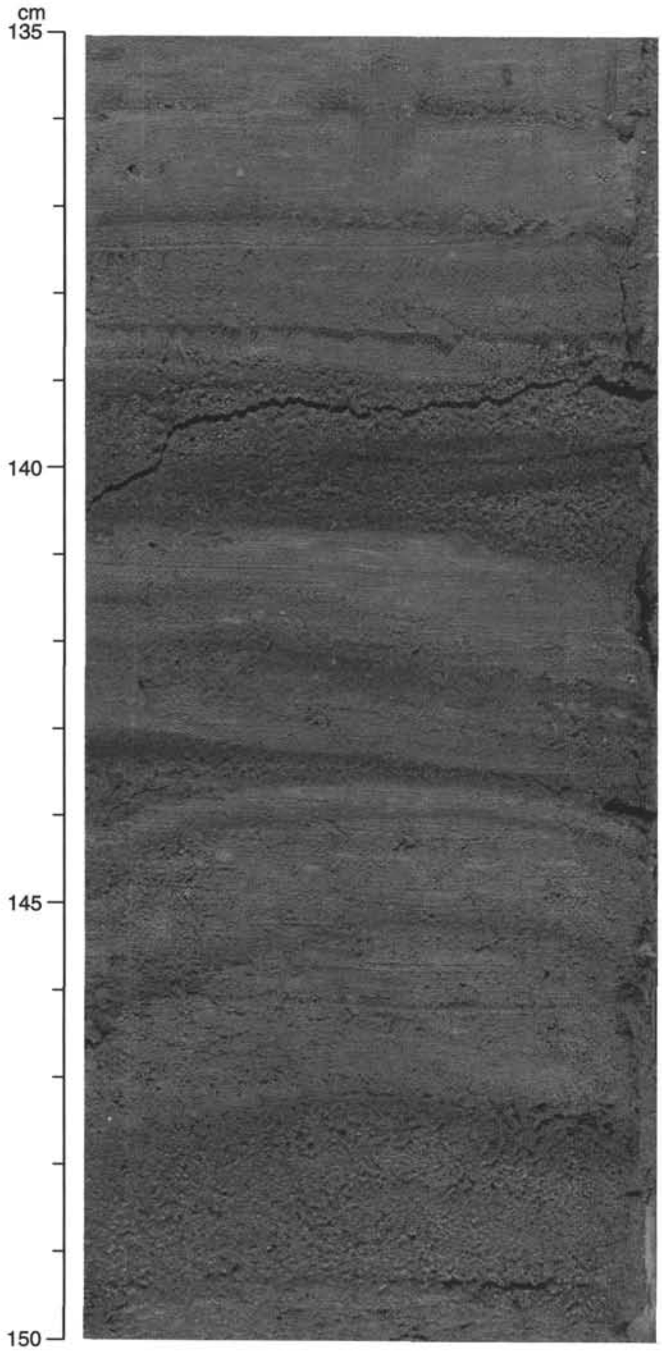

Figure 8. Volcanic ash fall layer within a section of nannofossil ooze. Note the parallel lamination. Interval 157-954A-9H-1, 135–150 cm.

characteristic banded appearance to the deposits such as in Core 157-954B-13R-1. Depositional sequences usually begin with a crystal-lithic siltstone or sandstone at the base that grade upward into moderately to extensively bioturbated claystone. Each of these sequences is interpreted as a single turbidite deposit.

The interval between Cores 157-954B-17R and 157-954B-30R is characterized by the presence of spectacular soft sediment slump structures (i.e., liquefied beds, flame structures; Fig. 11). Some deformation, however, occurred after lithification of the sediment as indicated by small faults and brecciation within this unit (Fig. 12).

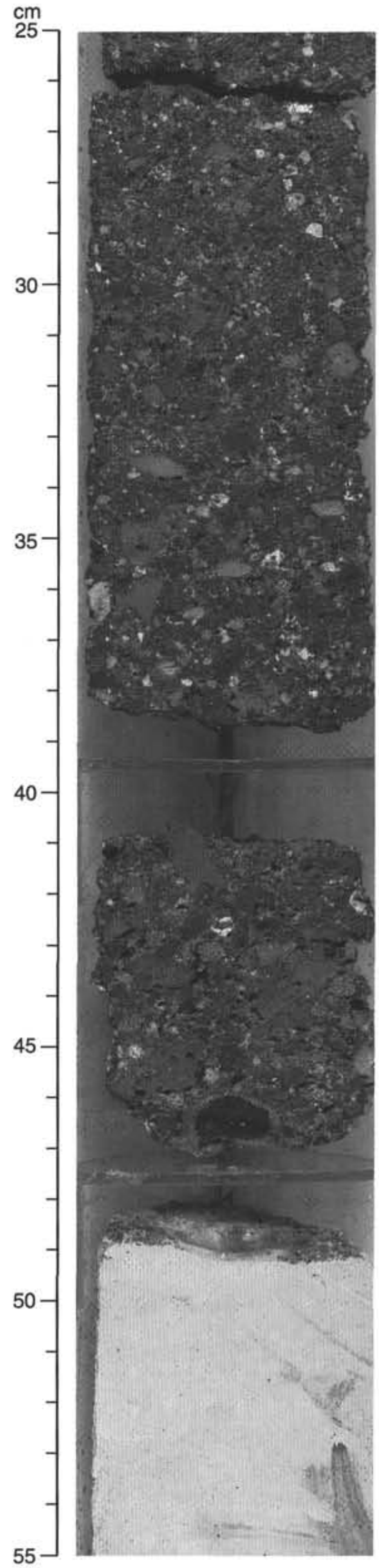

Figure 9. Lapillistone recovered in Unit II showing its contact with underlying nannofossil chalk. Note the fining-upward grading. Interval 157-954B-11R-2, 25–55 cm.

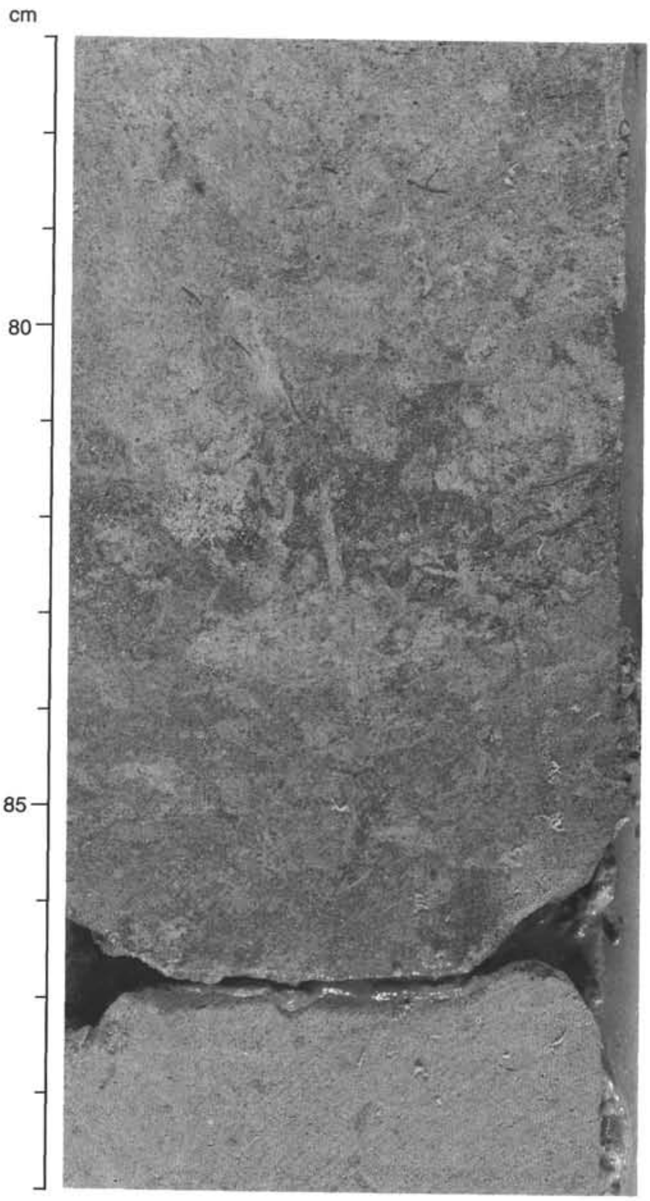

Figure 10. Bioturbated nannofossil chalk bed of Unit III with dispersed dark fine-grained lithic and crystal particles. Interval 157-954B-22R-3, 77–89 cm.

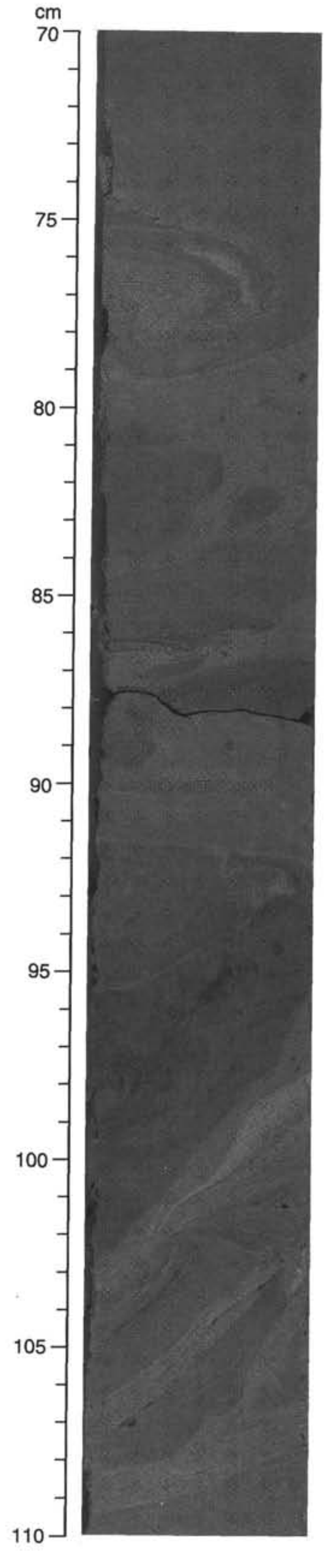

Figure 11. Soft sediment deformation in Unit III. Note the presence of folds, sheared and brecciated beds, and flame structures. Interval 157-954B-27R-3, 70–110 cm.

Unit IV

Interval: Sections 157-954B-35R-1 to 157-954B-39R-2
Depth: 408–446 mbsf
Age: middle Miocene (14 Ma)

Unit IV is 38 m thick, and a hiatus occurs between Units III and IV. The unit comprises exclusively dark green to gray basaltic breccia. The breccia is structureless, very poorly sorted, and may constitute a single thick unit, although boundaries between units may have been lost during coring. Large basalt fragments within the breccia are both matrix- and clast-supported at various levels in the unit, with the former being more common. The clasts consist of moderately vesicular and nonvesicular olivine-clinopyroxene and minor plagioclase-phyric basalt, and mostly nonvesicular aphyric basalt. Olivine is generally altered, but fresh olivine occurs in some clasts. Vesicular clasts are more abundant than nonvesicular ones. Some smaller clasts are

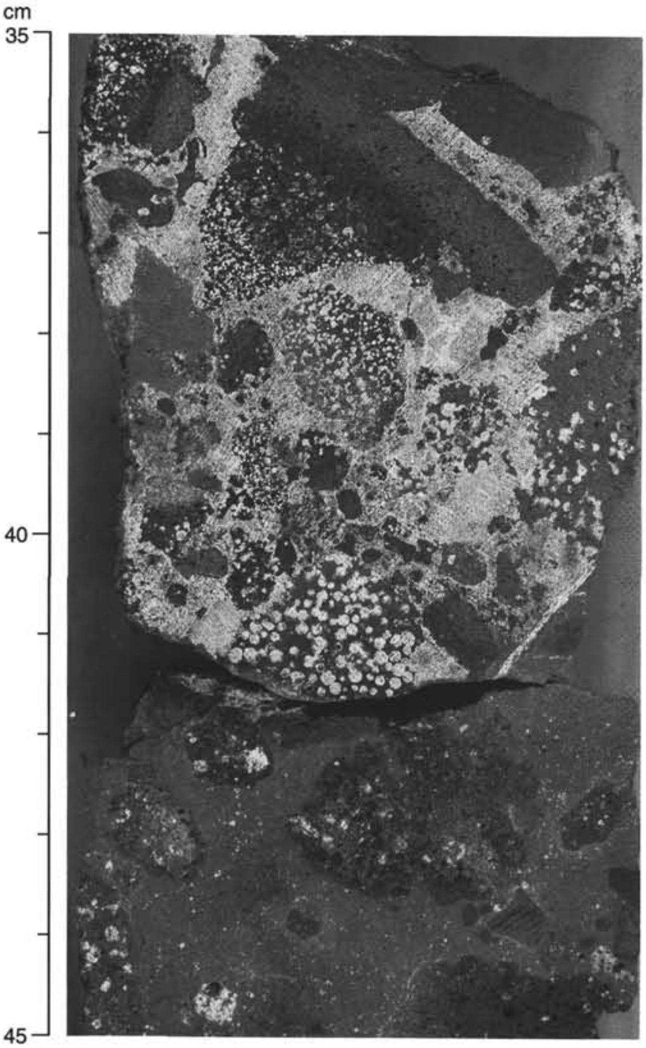

Figure 12. Volcanic breccia of Unit IV. Note the vesiculation of volcanic clasts and the pillow fragment at the top of the photograph. Interval 157-954B-38R-3, 35–45 cm.

orange (oxidized), suggesting subaerial exposure. In Core 157-954B-34R an unusual clast of dark gray, mafic tuff contains accretionary lapilli up to 5 mm in diameter.

The majority of basalt clasts are subangular to subrounded and range up to 22 cm in diameter based on the their length in the cores. However, some fragments are angular. For example, in Core 157-954B-39R several angular clasts of vesicular pillow basalt with remnant quenched rims are found (Fig. 12). Smaller clasts consist of vesicular and nonvesicular crystalline basalt, crystals of altered olivine, clinopyroxene, and Fe-Ti oxides, and moderately vesicular hyaloclastite fragments. Most of the hyaloclastite fragments have been completely altered to greenish clay minerals or zeolites.

The matrix of this unit consists of green noncalcareous clay and/or zeolites and grayish-white calcareous clay. In addition, the unit is cut by numerous thin veins composed of calcite.

Depositional History

The poor sorting, matrix-support of clasts, and structureless character of Unit IV suggest emplacement by one or more debris flows. Furthermore, the polymict nature of the deposit, abundance of vesicular and oxidized clasts, and subrounded nature of many fragments may indicate a subaerial volcanic source. Hyaloclastite fragments and clasts of pillow basalts are evidence that the breccia is a mixture of subaerially derived and shallow-water volcanics, as they typically occur during the emergent phase of volcanic islands. These breccias resemble those of Unit VI at Site 953. No sediments corresponding to the Fataga or Mogan phase, on Gran Canaria are present between Units III and IV indicating that there is a large as yet unexplained hiatus between ~10.7 and ~14 Ma. Unit IV probably represents a breccia emplaced at ~14 Ma after completion of the basaltic shield at the beginning of the Mogan phase.

For the next 6 m.y. (Unit III) sedimentation was dominated by the pelagic deposition of nannofossil ooze and nannofossil mixed sediment punctuated by the influx of volcaniclastic sand, silt, and clay in the form of turbidity currents. This period corresponds to the volcanic hiatus on Gran Canaria (4.5–9.5 Ma; Schmincke, 1994) and follows the Fataga phase of volcanism that produced relatively large volumes of phonolitic magma. Some of the turbidite deposits of Unit III contain phonolitic clasts and minerals such as biotite, alkali feldspar, and amphibole, which are characteristic of the Fataga activity and thus likely represent the eroded subaerial products.

A distinctive feature of Unit III is the occurrence of a thick interval of slumped sediments at 302–359 mbsf. This sequence shows soft sediment deformation features indicating that slumping occurred while the sediments were unconsolidated. A similar thick sequence of slumped sediments of similar age occurs at Site 953 from ~321 to 388 mbsf. The slumped sequences at both sites are most likely correlative and represent a period of instability that affected a large part of the northern flank of Gran Canaria.

During the late Pliocene (~3.7 Ma), there was an influx of coarse phonolitic and basaltic volcaniclastic material to the site by debris flows (Unit II). High vesicularity of some of the clasts, presence of pumice, and absence of hyaloclastic particles in these lapillistones strongly suggest that the volcanic material was produced during subaerial volcanic activity. Moreover, the angularity of the clasts suggests rapid deposition.

Sedimentation of Unit II was contemporaneous with volcanic activity on Gran Canaria. Biostratigraphic age data (see "Biostratigraphy," this chapter), indicates that the emplacement of the lapillistone debris flows occurred during the Roque Nublo volcanic stage of Gran Canaria (3.5–4.3 Ma; Schmincke, 1994) and that these deposits are contemporaneous with the coarse volcaniclastics of Unit II in Site 953.

During the last 3.5 m.y., sedimentation was mainly pelagic and characterized by the deposition of nannofossil ooze and larger volumes of turbiditic calcareous sands (Fig. 4) derived from shallow-water carbonate sources. Dark volcanic sands resulting from erosion and reworking of mainly mafic epiclastic material from Gran Canaria occurred during the same period. The increase of calcareous bioclastic sedimentation during Unit I may reflect Pleistocene glacial–interglacial intervals and associated sea-level changes. Ash fall layers in Unit I of Site 954 are coarser and thicker than at Site 953, probably because Site 954 is located in the main fallout axis of explosive eruptions from Tenerife.

BIOSTRATIGRAPHY

Introduction

Sediments at Site 954 range in age from Quaternary to late or middle Miocene (Fig. 13). The sequence is interrupted by at least three hiatuses: the first in the lower Pleistocene and upper Pliocene about 1 to 1.9 Ma, in the lower Pliocene from roughly 4.4 to 5.3 Ma, and in the lower upper Miocene from roughly 8.8 to 9.4 Ma. Stratigraphically repeated sections appear in the Miocene and possible in the Pleistocene.

The pattern of preservation and abundance of calcareous nannofossils differs from that of planktonic foraminifers. Abundance of nannofossils is generally high to very high throughout the core. In

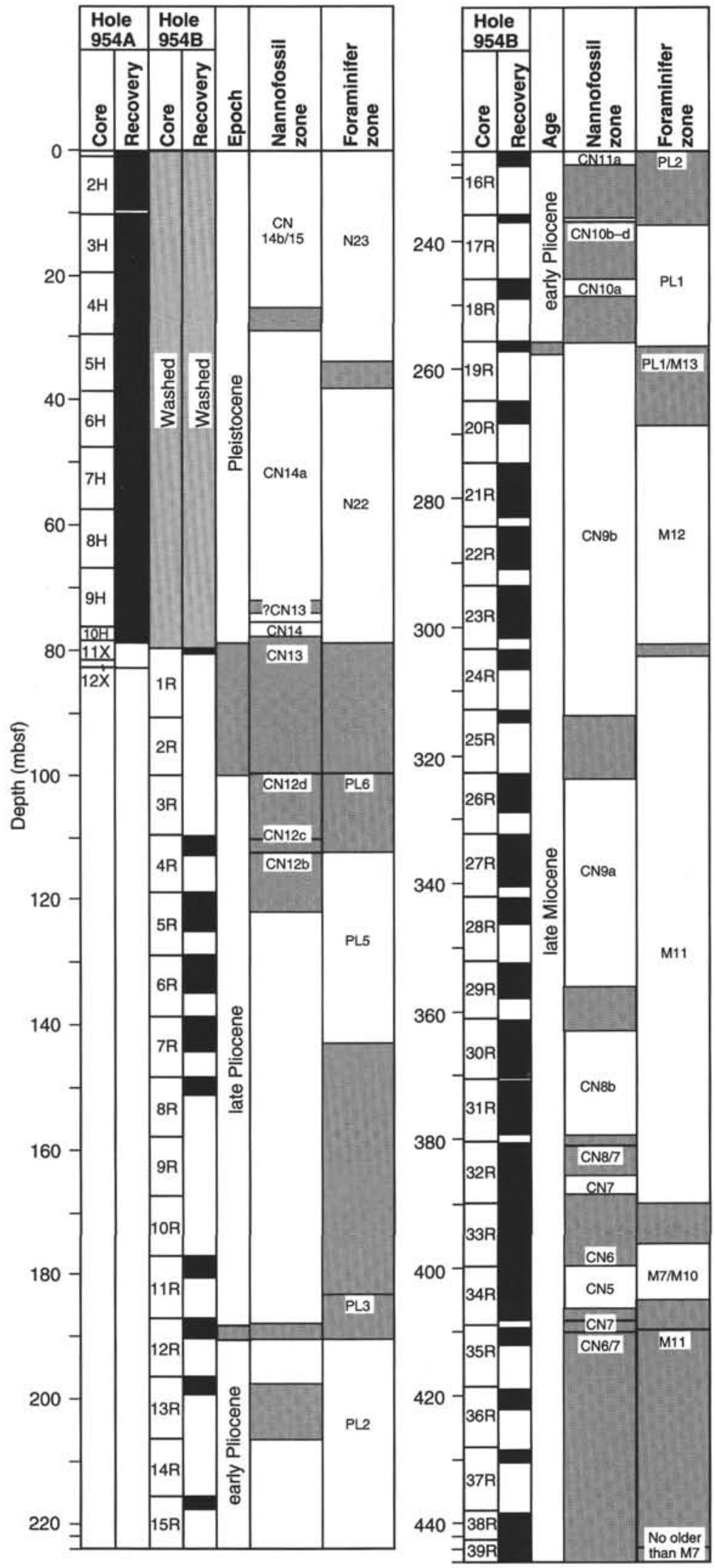

Figure 13. Nannofossil and foraminifer zonation at Site 954.

contrast, planktonic foraminifers are generally abundant only to the base of the Pliocene at about 255 mbsf and are few to common in abundance to the top of the basal basalt breccia. Foraminifers are abundant in several intervals within the breccia matrix. Calcareous nannofossils are generally well preserved throughout most of the sequence except for an interval of moderate preservation from 266 to 355 mbsf. Planktonic foraminifers, in contrast, are poorly preserved below 280 mbsf except in the basalt breccia where they are well preserved in the lithified matrix.

The Pliocene/Pleistocene boundary is placed between the highest occurrence of *Discoaster brouweri* in Sample 157-954B-3R-CC, 0–2 cm (100.10 mbsf), and the lowest occurrence of the planktonic foraminifer, *Globorotalia truncatulinoides* in Sample 157-954B-11X-1, 0–2 cm (79.20 mbsf). The Miocene/Pliocene boundary is placed at the highest occurrence of *Discoaster quinqueramus* (5.56 Ma) in Sample 157-954B-19R-1, 4 cm (254.14 mbsf), and is supported by the close proximity of the highest occurrence of *Globorotalia juanai* (5.4 Ma) in Sample 157-954B-19R-CC, 0–2 cm (255.37 mbsf).

Calcareous Nannofossils

Site 954 recovered approximately 407.96 m of Pleistocene to late Miocene and possibly middle Miocene age sediments representing Zones CN15 to CN5 (Table 2). Three hiatuses and two possible repeated sections were recognized.

Pleistocene

Well-preserved Pleistocene nannofossils were recovered from the surface to Sample 157-954B-1R-1, 122 cm (81.42 mbsf). The lowest occurrence of *Emiliania huxleyi* could not be determined positively with the light microscope, so all samples above the highest occurrence of *Pseudoemiliania lacunosa* in Sample 157-954A-4H-7, 8 cm (29.08 mbsf), which marks the top of Subzone CN14a, were assigned to undifferentiated Subzones CN14b/15. Within Subzone CN14a, the highest occurrence of *Reticulofenestra asanoi* occurred in Sample 157-954A-8H-4, 35 cm (62.85 mbsf). *R. asanoi* is absent in Sample 157-954A-9H-6, 97 cm (75.97 mbsf), which is dominated by small *Gephyrocapsa* spp. (<4 µm maximum diameter), but it reappears again in Sample 157-954A-10H-1, 32 cm (77.32 mbsf) suggesting a repeated section. Cores 157-954A-8H, 9H, and 10H contain numerous slumps that may have thickened this part of the section.

The lowest occurrence of *R. asanoi,* which approximates the base of Subzone CN14a, occurs in Sample 157-954A-10H-2, 12 cm (78.62 mbsf). The next lowest sample, 157-954A-11X-CC, 14 cm (79.34 mbsf), contains large *Gephyrocapsa* spp. (>4 µm maximum diameter). The highest occurrence of *Calcidiscus macintyrei,* occurs in Sample 157-954B-1R-1, 122 cm (81.42 mbsf). These two samples, below the lowest occurrence of *R. asanoi,* are assigned to undifferentiated Zone CN13.

Pliocene

The highest occurrence of *Discoaster brouweri* indicates Subzone CN12d in Sample 157-954B-3R-CC (100.10 mbsf) with an age of about 1.95 Ma. The first occurrence datum for *R. asanoi* occurs at 1.06 Ma, indicating that 2.80 m of sediment was deposited in 0.89 m.y. This anomalously low rate of sediment accumulation in conjunction with the repeated Subzone CN13b directly above, suggests a hiatus reflecting basinward slumping.

The highest occurrence of *D. pentaradiatus* occurs in Sample 157-954-4R-1, 69 cm (110.39 mbsf), indicating Subzone CN12c, with Subzone CN12b indicated in Sample 157-954B-4R-2, 105 cm (112.25 mbsf), by the highest occurrence of *D. surculus*; Subzone CN12a is indicated in Sample 157-954B-5R-2, 89 cm (121.69 mbsf), by the highest occurrence of *D. tamalis.* The very poor recovery and dolomitization present in Cores 157-954B-9R and 10R occurred within Subzone CN12a and so did not affect biostratigraphic resolution. Early Pliocene Subzone CN11b is found in Sample 157-954B-12R-CC (190.18 mbsf) by the highest co-occurrence of *Reticulofenestra pseudoumbilicus* and *Sphenolithus* spp. The base of Subzone CN11b, marked by the lowest occurrence of *D. tamalis,* occurs in Sample 157-954B-13R-1, 71 cm (197.21 mbsf).

The highest occurrence of *Amaurolithus* spp. in Sample 157-954B-17R-1, 16 cm (234.96 mbsf), indicates Zone CN10. Poor recovery of core and the absence of marker species prevented us from determining Subzones CN10b–d. Subzone CN10a was indicated by the highest occurrence of *Triquetrorhabdulus rugosus* in Sample 157-954B-18R-1, 33–34 cm (244.73 mbsf). A hiatus at 4.4–5.3 Ma between Samples 157-954B-17R-1, 58 cm (235.38 mbsf), and 157-954B-18R-1, 33–34 cm (244.73 mbsf), is suggested by the last occurrence of *Amaurolithus* spp. at 234.96 mbsf and the highest occurrence of *T. rugosus* at 244.73 mbsf. These two events representing approximately 0.9 m.y. occur over 9.34 m, which indicates an accumulation rate of about 10 m/m.y. This rate is relatively low and suggests either a condensed zone or, more likely, a hiatus.

Miocene

The highest occurrence of *Discoaster quinqueramus* in Sample 157-954B-19R-1, 4 cm (254.14 mbsf) indicates Subzone CN9b in the late Miocene. Three useful events occur within Subzone CN9b: the highest and lowest occurrences of *Amaurolithus amplificus* in Samples 157-954B-20R-1, 95 cm (264.65 mbsf), and 157-954B-22R-4, 62 cm (287.92 mbsf), and the top of the paracme of large *Reticulofenestra pseudoumbilicus* (>7 µm maximum diameter) in Sample 157-594B-23R-6, 26 cm (300.16 mbsf). The lowest occurrence of *A. primus* in Sample 157-954B-25R-1, 48 cm (312.18 mbsf) defines the base of CN9b. The lowest occurrences of *D. quinqueramus* and *D. berggrenii* mark the base of CN9a in Sample 157-954B-29R-4, 96 cm (355.35 mbsf).

Discoaster loeblichi and *D. neorectus,* the primary markers for the subzones of Zone CN8, were not found at this site. However, another event, the reentrance of large *Reticulofenestra pseudoumbilicus* (>7 µm maximum diameter), which occurs within the lower part of CN8b (Rio et al., 1990; Young, 1990; Young et al., 1994) at about 8.8 Ma, proved useful. The samples above the highest occurrence of the reentrance of large *R. pseudoumbilicus* in Sample 157-954B-31R-6, 118.5 cm (377.83 mbsf), were placed in Subzone CN8b. The sample below the reentrance of large *R. pseudoumbilicus,* Sample 157-954B-32R-1, 93 cm (379.83 mbsf), contains the lowest occurrence of *Minylitha convallis,* an event that usually occurs in the upper part of Zone CN7 (Rio et al., 1990; Gartner, 1992), at approximately 9.4 Ma. The occurrence of these two events, the reentrance of large *R. pseudoumbilicus* and the FO of *M. convallis,* dated as 8.8 and 9.4 Ma, within 2 m, suggests a short hiatus that spans ~600 ka.

The highest occurrence of *Discoaster hamatus* in Sample 157-954B-32R-4, 105 cm (384.26 mbsf), marks Zone CN7. Sample 157-954B-33R-1, 7 cm (388.57 mbsf), has the lowest occurrence of *D. hamatus,* marking the base of Zone CN7. Sample 157-954B-33R-CC, 6 cm (398.07 mbsf), contains the lowest occurrence of *Catinaster coalitus* without *D. hamatus* and indicates CN6. Samples 157-954B-34R-1, 16 cm (398.26 mbsf), 157-954B-34R-2, 61.5 cm (400.22 mbsf), and 157-954B-34R-6, 11 cm (405.71 mbsf), contain *Coccolithus miopelagicus* without the younger species *Catinaster coalitus* or *D. hamatus,* which indicates Zone CN5. However, in Sample 157-954B-35R-1, 3 cm (407.83 mbsf), Zone CN7 is repeated with the reappearance of *D. hamatus.* The deepest sample to contain nannofossils was Sample 157-954B-35R-1, 16 cm (407.96 mbsf). This sample contained *C. coalitus* without *D. hamatus,* suggesting Zone CN6. However, 5-rayed discoasters similar to *D. bellus,* which has a FO datum nearly coincident with that of *D. hamatus* were also

Table 2. Abundance, preservation, and lithology of samples used in nannofossil zonation, Holes 954A and 954B.

Core, section, interval (cm)	Depth (mbsf)	Abundance	Preservation	Zone	Lithology
157-954A-					
1H-1, 4–4	0.04	VH	G	CN14b/15	Hemipelagic ooze
1H-CC, 0–0	0.86	VH	G	CN14b/15	Hemipelagic ooze
2H-1, 6.5–6.5	1.07	H	G	CN14b/15	Hemipelagic ooze
3H-6, 101–101	19.01	VH	G	CN14b/15	Hemipelagic ooze
4H-4, 60–60	25.10	VH	G	CN14b/15	Hemipelagic ooze
4H-7, 8–8	29.08	VH	G	CN14a	Hemipelagic ooze
4H-CC, 0–0	29.27	VH	G	CN14a	Hemipelagic ooze
6H-1, 38–38	39.38	VH	G	CN14a	Hemipelagic ooze
7H-1, 25–25	48.75	VH	G	CN14a	Hemipelagic ooze
8H-2, 18–18	59.68	VH	G	CN14a	Hemipelagic ooze
8H-3, 120–120	62.20	VH	G	CN14a	Hemipelagic ooze
8H-4, 35–35	62.85	VH	G	CN14a	Turbidite
8H-4, 74–74	63.24	VH	G	CN14a	Hemipelagic ooze
8H-CC, 0–0	67.64	H	G	CN14a	Hemipelagic ooze
9H-1, 116–116	68.66	VH	G	CN14a	Hemipelagic ooze
9H-2, 149–149	70.49	VH	G	CN14a	Hemipelagic ooze
9H-4, 60–60	72.60	VH	G	CN14a	Hemipelagic ooze
9H-6, 97–97	75.97	VH	G	?CN13b	Hemipelagic ooze
10H-1, 32–32	77.32	VH	G	CN14a	Hemipelagic ooze
9H-CC, 0–0	77.40	VH	G	CN14a	Hemipelagic ooze
10H-1, 66–66	77.66	VH	G	CN14a	Hemipelagic ooze
10H-2, 12–12	78.62	VH	G	CN14a	Hemipelagic ooze
11X-CC, 14–14	79.34	VH	G	CN13	Hemipelagic ooze
157-954B-					
1R-1, 122–122	81.42	M	P	CN13	Lapillistone matrix
3R-CC, 0–0	100.10	VH	M	CN12d	Hemipelagic ooze
4R-1, 69–69	110.39	VH	G	CN12c	Hemipelagic ooze
4R-2, 105–105	112.25	H	G	CN12b	Hemipelagic ooze
4R-CC, 0–0	112.68	VH	G	CN12b	Hemipelagic ooze
5R-2, 89–89	121.69	VH	G	CN12a	Hemipelagic ooze
5R-4, 24–24	124.04	VH	G	CN12a	Hemipelagic ooze
6R-3, 12–12	132.12	VH	M	CN12a	Hemipelagic claystone
7R-4, 55–55	143.65	VH	G	CN12a	Hemipelagic ooze
8R-2, 105–105	150.55	VH	M	CN12a	Hemipelagic ooze
9R-CC, 0–0	158.00	VL	P	CN12a	Dolostone
11R-3, 6–6	179.97	VH	G	CN12a	Hemipelagic chalk
12R-1, 89.5–89.5	187.80	M	G	CN12a	Turbidite?
12R-CC, 0–0	190.18	H	G	CN11b	Hemipelagic claystone
13R-1, 71–71	197.21	H	M	CN11b	Hemipelagic chalk
14R-CC, 5.5–5.5	206.26	H	M	CN11a	Hemipelagic claystone
15R-2, 26–26	217.11	H	M	CN11a	Hemipelagic chalk
16R-2, 40–40	227.10	VH	M	CN11a	Hemipelagic claystone
17R-1, 16–16	234.96	VH	G	CN10b d	Hemipelagic chalk
17R-1, 58–58	235.38	VH	G	CN10b d	Turbidite
18R-1, 33–34	244.73	VH	G	CN10a	Hemipelagic chalk
18R-CC, 0–0	247.40	VH	G	CN10a	Hemipelagic chalk
19R-1, 4–4	254.14	VH	G	CN9b	Hemipelagic chalk
19R-CC, 71–71	256.09	H	G	CN9b	Turbidite?
20R-1, 95–95	264.65	VH	G	CN9b	Hemipelagic chalk
20R-2, 140–140	266.60	VH	M	CN9b	Hemipelagic chalk
21R-1, 43–43	273.73	VH	M	CN9b	Hemipelagic chalk
21R-4, 57–57	278.37	H	M	CN9b	Hemipelagic chalk
21R-6, 28–28	281.08	H	M	CN9b	Hemipelagic chalk
22R-4, 62–62	287.92	VH	M	CN9b	Hemipelagic chalk
23R-1, 112–112	293.52	VH	M	CN9b	Hemipelagic chalk
23R-6, 26–26	300.16	H	M	CN9b	Hemipelagic chalk
24R-2, 88–88	304.36	H	M	CN9b	Hemipelagic chalk
25R-1, 48–48	312.18	H	M	CN9b	Hemipelagic chalk
26R-1, 78–78	322.18	H	M	CN9a	Hemipelagic chalk
26R-5, 8– 8	327.48	H	M	CN9a	Hemipelagic chalk
27R-4, 33–33	335.93	H	M	CN9a	Hemipelagic claystone
28R-3, 89–89	344.43	H	M	CN9a	Hemipelagic claystone
29R-4, 96–96	355.35	M	M	CN9a	Turbidite?
30R-2, 26–26	361.57	M	P	CN8b	Hemipelagic claystone
30R-7, 104–104	369.06	M	P	CN8b	Hemipelagic claystone
31R-1, 70–70	370.10	H	G	CN8b	Hemipelagic claystone
31R-6, 118.5–118.5	377.83	L	P	CN8b	Hemipelagic claystone
32R-1, 93–93	379.83	VH	G	CN8	Hemipelagic claystone
32R-4, 105–105	384.26	H	G	CN7	Hemipelagic claystone
32R-7, 51–51	387.99	H	G	CN7	Hemipelagic chalk
33R-1, 7–7	388.57	H	G	CN7	Turbidite
33R-CC, 6–6	398.07	VH	G	?CN6	Hemipelagic chalk
34R-1, 16–16	398.26	VH	G	?CN5	Hemipelagic chalk
34R-2, 61.5–61.5	400.22	M	M	?CN5	Hemipelagic chalk
34R-6, 11–11	405.71	H	G	?CN5	Hemipelagic chalk
35R-1, 3–3	407.83	VH	G	CN7	Hemipelagic chalk
35R-1, 16–16	407.96	M	P	CN6/7	Hemipelagic chalk
35R-1, 46–46	408.26	B			Breccia matrix
35R-2, 146–146	410.76	B			Dolostone
36R-2, 67.5–67.5	419.41	B			Breccia matrix
37R-2, 52–52	428.82	B			Breccia matrix
38R-3, 48.5–48.5	439.72	VL	P		Breccia matrix
38R-4, 17–17	440.84	B			Breccia matrix
39R-2, 32–32	442.93	B			Breccia matrix

Note: Key to abbreviations for abundance and preservation in "Explanatory Notes" (this volume).

present suggesting Zone CN7. Because of this uncertainty, this sample was assigned to undifferentiated Zone CN6/7. A similar repeated sequence is seen in the foraminifer data.

There are several possible explanations for this sequence:

1. The Zone CN7 and CN6/7 material sampled in Samples 157-954B-35R-1, 3 cm (407.83 mbsf), and 157-954B-35R-1, 16 cm (407.96 mbsf), could have fallen from higher in the hole. These samples were from a short pelagic section less than 20 cm long above basaltic breccias so the age of the base of the fossiliferous section could be as old as CN5 at 405.71 mbsf.
2. The older material of Zone CN5 was reworked by turbidites. In this case the age of the deepest fossiliferous sediments at 407.96 mbsf would be Zone CN6 or CN7.
3. The repeated section is caused by slumping. With this interpretation, the deepest fossiliferous sediments again indicate Zone CN6 or CN7 at 407.96 mbsf. The nannofossil evidence alone does not allow us to distinguish between these possibilities.

Planktonic Foraminifers

Planktonic foraminifers are well preserved and abundant throughout Hole 954A and uppermost Hole 954B to Sample 157-954B-8R-CC, 0–2 cm (150.90 mbsf), moderately preserved and abundant or common to Sample 157-954B-20R-CC, 0–2 cm (267.07 mbsf), and poorly preserved and mostly few in abundance to Sample 157-954B-35R-1, 2–4 cm (407.81 mbsf) (Table 3). Well-preserved foraminifers occur in the matrix of the basalt breccia, though they must be viewed in thin section. All zones from N23 to M11 were represented (Fig. 13), except Zone M13 near the Pliocene/Miocene boundary. Several intervals in the Pleistocene, Pliocene, and Miocene, however, suffered from poor core recovery, which truncated several zones.

The base of Zone N22 between Samples 157-954A-11X-1, 0–2 cm (79.20 mbsf), and 157-954B-3R-CC, 0–2 cm (100.09 mbsf), lies below the Pleistocene-Pliocene hiatus. The PL1/M13 boundary between Samples 157-954B-19R-1, 49–51 cm, and 157-954B-20R-CC, 0–2 cm (254.58–267.07 mbsf), is uncertain because Zone M13 was not unambiguously recognized. A repeated interval occurs at the base of the hole above the basal basalt breccia. A sample assigned to Zone M11 (Sample 157-954B-35-1, 2–4 cm, 407.83 mbsf) beneath two samples (Samples 157-954B-33R-5, 10–12 cm, and 157-954B-34R-4, 51–53 cm) derives from the undifferentiated Zone M7/M10.

Quaternary

The Quaternary sequence was divided into Zone N23 based on the range of *Globigerina calida calida* and Zone N22 between the first appearances of *Globorotalia truncatulinoides* and *Globigerina calida calida* (Fig. 13). The interval contained a diverse assemblage typical of subtropical waters including abundant *Globigerinoides ruber, Globigerinella aequilateralis, Globigerinoides sacculifer,* and *Globorotalia crassaformis.* Climatic fluctuations were indicated by the alternation of warm subtropical assemblages with *Pulleniatina obliquiloculata* and cool subtropical assemblages with abundant dextral *Neogloboquadrina pachyderma* and *Globorotalia inflata.* We suspect that the lower part of Zone N22 was not recovered and may have been disrupted by a condensed interval between 78.62 and 79.34 mbsf. This is suggested by the nannofossil data and by the emplacement of a lapillistone, the top of which lies at 80.2 mbsf.

Pliocene

The Pliocene interval ranged from PL6 to PL1, and the assemblages were well-preserved, abundant, and diverse (Table 3). The uppermost Pliocene sample (Sample 157-954B-3R-CC, 0–2 cm, 100.09 mbsf) was assigned to the lower part of Zone PL6 between the first appearance of *Globorotalia inflata* and the reappearance of *Pulleniatina* in the North Atlantic Ocean. The upper part of the zone was not recovered from the overlying interval of volcaniclastic material in Cores 157-954B-11X to 157-954B-4R, which suffered from very poor core recovery. Samples 157-954B-4R-CC, 0–2 cm, to 157-954B-7R-CC, 0–2 cm (112.67–144.18 mbsf) were placed in Zone PL5 based on the occurrence of *Globorotalia miocenica* without *Globorotalia multicamerata.* The uppermost sample from this interval (Sample 157-954B-4R-CC, 0–2 cm) also contained *Globorotalia truncatulinoides,* which is interpreted as contamination of the core catcher with sediment from the upper part of the hole.

Poor core recovery may have truncated the next two zones. Core 157-954B-9R contained only a nannofossil-bearing dolostone, and Core 157-954B-10R had no recovery at all. Zone PL4 was found in only one sample (Sample 157-954B-8R-CC, 0–2 cm, 150.90 mbsf) above the interval of poor core recovery. The zone is marked by the occurrence of common *Globorotalia multicamerata* with rare *Globoquadrina altispira.* Zone PL3 was found in only one sample (Sample 157-954B-11R-CC, 0–2 cm) below the interval of poor recovery. The zone was marked by the occurrence of *Sphaeroidinellopsis seminulina* without *Globorotalia margaritae.*

Zone PL2 extended from Sample 157-954B-12R-CC, 0–2 cm, to Sample 157-954B-16R-CC, 0–2 cm, and was indicated by the occurrence of *Globorotalia margaritae* without *Globigerina nepenthes.* Zone PL1 found in Samples 157-954B-17R-CC, 0–2 cm (235.69 mbsf), to 157-954B-19R-1, 49–51 cm (254.58 mbsf), was based on the occurrence of *Globigerina nepenthes* and *Globorotalia margaritae* without *Globorotalia juanai* or other species restricted to the Miocene.

Miocene

The PL1/M13 boundary lies between Samples 157-954B-19R-1, 49–51 cm (254.58 mbsf), and 157-954B-20R-CC, 0–2 cm (267.07 mbsf), the latter of which bears frequent *Globorotalia juanai.* The intermediate sample, 157-954B-19R-CC, 0–2 cm, contains only one specimen of *Globorotalia juanai* with an assemblage typical of PL1 including *Globorotalia margaritae,* so we placed it tentatively in undifferentiated Zones PL1/M13. No other samples were seen that could be assigned to Zone M13. With further work, we may assign part of this interval to Zone M13. We used the secondary marker species, *Globorotalia juanai,* to define the top of M13 because the defining marker, *Globoquadrina dehiscens,* is essentially absent from the region after about 10 Ma.

Zone M12 was recognized in Samples 157-954B-20R-CC, 0–2 cm (267.07 mbsf), to 157-954B-23R-CC, 0–2 cm (300.85 mbsf), by the presence of *Globorotalia conomiozea* with sinistral *Neogloboquadrina acostaensis* and without *Globorotalia margaritae.* Preservation was very poor in samples below 280 mbsf in the middle of Zone M12, so zonal assignment was more tentative. Zone M11 was recognized from Samples 157-954B-24R-1, 96–97 cm (302.95 mbsf), to 157-954B-32R-7, 88–90 cm (388.35 mbsf), with the presence of *Neogloboquadrina acostaensis* and *Globigerina nepenthes* without *Globorotalia conomiozea.* Other taxa found sporadically in the interval include *Globorotalia plesiotumida, Sphaeroidinellopsis seminulina, Orbulina* sp., *Globoquadrina baroemoenensis, Globorotalia menardii menardii, Globorotalia miozea,* and *Globigerinoides obliquus.*

Samples 157-954B-33R-5, 10–12 cm (394.59 mbsf), and 157-954B-34R-4, 51–53 cm (403.10 mbsf), are assigned to the undifferentiated Zone M7/M10. The upper sample contains *Globoquadrina dehiscens, Globorotalia continuosa, Globorotalia siakensis,* and *Paragloborotalia mayeri,* and the lower sample contains an impoverished assemblage with only *Paragloborotalia mayeri* and *Orbulina universa.* The samples clearly contain an assemblage older than M11. The sample underlying this interval, Sample 157-954B-35R-1, 2–4 cm (407.81 mbsf), bears globorotalids similar to those found in Zone M11, *Globorotalia menardii menardii* and *Globorotalia plesiotumi-*

Table 3. Abundance, preservation, and lithology of samples used in foraminifer zonation.

Core, section, interval (cm)	Depth (mbsf) Top	Bottom	Abundance	Preservation	Zone	Lithology
157-954A-						
1H-1, 0–1	0.00	0.01	A	G	N23	Brown ooze
1H-CC, 0–2	0.85	0.87	A	G	N23	Brown ooze
2H-CC, 0–2	9.65	9.67	F	P	N23?	Black ash
3H-2, 61–63	12.60	12.62	A	G	N23	Calcareous sand
3H-CC, 0–2	19.49	19.51	F	M	N23?	Pumice pebble sand
4H-CC, 0–2	29.26	29.28	A	G	N23	Pelagic ooze
5H-4, 16–18	34.15	34.17	A	G	N23	Pelagic ooze
5H-CC, 0–2	38.93	38.95	F	M	N22?	Calcareous sand
6H-2, 47–49	40.96	40.98	A	G	N22	Pelagic ooze
6H-CC, 0–2	48.22	48.24	F	P	N22	Pelagic ooze
7H-7, 30–32	57.79	57.81	A	G	N22	Pelagic ooze
7H-CC, 0–2	58.05	58.07	F	M	N22	Black beach sand
8H-CC, 0–2	67.63	67.65	C	M	N22	Pelagic ooze
9H-CC, 0–2	77.39	77.41	A	M	N22	Pelagic ooze
10H-1, 29–32	77.27	77.30	A	G	N22	Pelagic ooze
11X-1, 0–2	79.20	79.22	A	G	N22	Pelagic ooze
157-954B-						
3R-CC, 0–2	100.09	100.11	A	G	PL6	Pelagic ooze
4R-CC, 0–2	112.67	112.69	A	G	PL5?	Pelagic ooze
5R-CC, 0–2	125.60	125.62	A	G	PL5	Pelagic ooze
6R-CC, 0–2	134.99	135.01	A	G	PL5	Turbidite
7R-CC, 0–2	144.18	144.20	A	G	PL5	Pelagic ooze
8R-CC, 0–2	150.90	150.92	A	G	PL4	Pelagic ooze
11R-CC, 0–2	180.26	180.28	A	M	PL3	Highly fractured chalk
12R-CC, 0–2	190.17	190.19	A	M	PL2	Pelagic ooze
13R-CC, 0–2	199.22	199.24	A	M	PL2	Pelagic ooze
14R-CC, 0–2	206.19	206.21	A	M	PL2	Pelagic ooze
15R-CC, 0–2	217.85	217.87	A	M	PL2	Pelagic ooze
16R-CC, 0–2	227.23	227.25	F	M	PL2	Turbidite
17R-CC, 0–2	235.69	235.71	A	M	PL1	Contorted nannofossil chalk
18R-CC, 0–2	247.39	247.41	C	M	PL1	Nannofossil chalk
19R-1, 49–51	254.58	254.60	A	M	PL1	Chalk with volcanic grains
19R-CC, 0–2	255.37	255.39	C	M	PL1/M13	Contorted chalk
20R-CC, 0–2	267.07	267.09	C	M	M12	Pelagic chalk
21R-3, 70–72	276.99	277.01	F	M	M12	Hemipelagic ooze
21R-CC, 0–2	281.95	281.97	F	P	M12	Hemipelagic mud
22R-CC, 0–2	289.46	289.48	F	P	M12	Hemipelagic mud
23R-CC, 0–2	300.85	300.87	F	P	M12	Hemipelagic mud
24R-1, 96–97	302.95	302.96	F	P	M11?	Hemipelagic mud
25R-CC, 0–2	313.45	313.47	C	P	M11?	Hemipelagic mud
26R-5, 0–2	327.39	327.41	C	P	M11	Hemipelagic mud
27R-6, 19–20	338.78	338.79	C	P	M11	Hemipelagic mud
28R-3, 81–84	344.34	344.37	C	P	M11	Hemipelagic mud
29R-4, 61–62	354.99	355.00	F	P	?	Hemipelagic mud
30R-7, 105–107	369.06	369.08	A	P	M11	Hemipelagic mud
31R-6, 90–92	377.53	377.55	R	P	M11	Hemipelagic mud
32R-7, 88–90	388.35	388.37	F	P	M11?	Hemipelagic mud
33R-5, 10–12	394.59	394.61	F	P	M7/M10	Turbidite
34R-4, 51–53	403.10	403.12	R	P	M7/M10	Turbidite
35R-1, 2–4	407.81	407.83	F	P	M11?	Hemipelagic mud
39R-2, 12–17	442.77	442.79	A	G	M7 or less	Matrix in basalt breccia
39R-2, 38–42	442.98	443.00	A	G	M7 or less	Matrix in basalt breccia

Note: Key to abbreviations for abundance and preservation in "Explanatory Notes" (this volume).

da, but no *Neogloboquadrina acostaensis.* We believe that the sample belongs in Zone M11. The results are supported by the calcareous nannofossil biostratigraphy, but the cause of the repeated interval of Zone M11 is unclear at this time (see discussion of nannofossils, this section, for details).

Thin sections of the basalt breccia at the base of the hole, Samples 157-954B-39R-2, 38–42 cm, and 157-954B-39R-2, 17–21 cm, contain a rich assemblage of planktonic foraminifers in the matrix. The few taxa identified are *Orbulina universa, Globoquadrina altispira, Globoquadrina dehiscens,* and *Globigerinoides trilobus.* The samples can be no older than M7 based on the occurrence of *Orbulina universa.*

PALEOMAGNETISM

Introduction

Paleomagnetic measurements of the NRM after demagnetization to 25 mT were made on the APC cores from Hole 954A and the RCB cores from Hole 954B. The APC cores from provided a partial magnetostratigraphic record for the almost 83 m drilled at this hole. The rotary cores gave only an incomplete record, which was further obfuscated by the presence of substantial slumping and lapillistones with coarse clasts. However, the paleontological age–depth determinations were sufficiently precise that we could match some magnetic features and build up a magnetostratigraphy over limited intervals. Discrete samples were not analyzed at this site because the lithologies are similar to those found at Site 953.

Hole 954A

Plots of inclination from all measurements and from undisturbed pelagic interbeds, with interpreted chron boundaries, are shown in Figure 14 (0–80 mbsf) and the depths of the various chron boundaries are given in Table 4. The intensity and the susceptibility results from MST measurements are shown in Figure 15 (0–80 mbsf).

The onset of the Brunhes is clearly seen between 50.5 and 51 mbsf. A synchronous declination and inclination change, with an as-

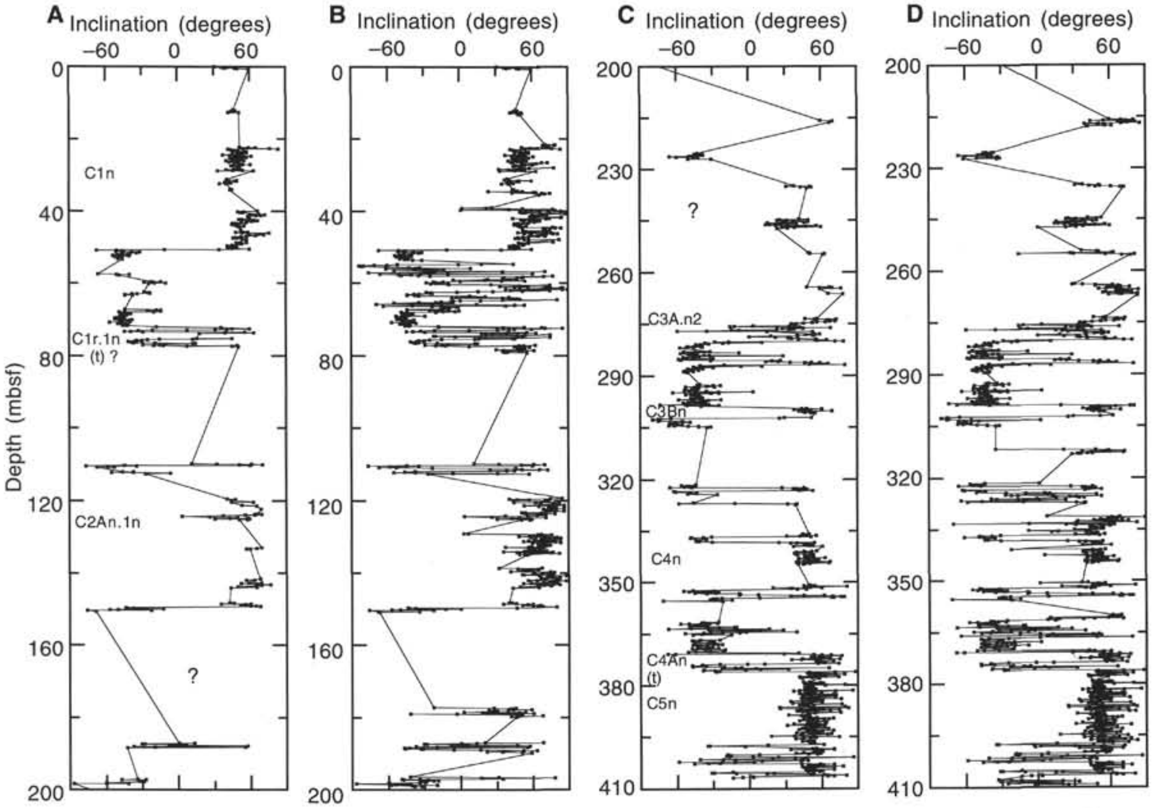

Figure 14. Magnetic data, NRM (25 mT), and interpreted polarity chrons from APC cores from Hole 954A, and RCB cores from Hole 954B. **A, C.** Inclination data from undisturbed pelagic intervals. **B, D.** Inclination data from all available intervals only.

sociated intensity low are all seen in interval 157-954A-7R-2, 55–105 cm. The synchronous change in declination and inclination at the time of the reversal suggests that the drill contamination is not important in this interval of core.

Two prominent intervals of reversed polarity are seen from 51 to 53 mbsf and from 68 to 72 mbsf. These are interpreted as manifestations of C1r (Matuyama). Between them lies a confusing interval of mixed polarities, which are correlated to coarse sand layers and drilling disturbances. The lower reversed interval lies above a predominantly normal interval, which is interpreted to be part of C1r.1n (Jaramillo), but we are unable to give a precise top to the subchron. The intensity of NRM and the susceptibility shown in Figure 15 exhibit fine-scale correlation that can be traced between the various lithologies as observed at the earlier sites.

Hole 954B

Continuing plots of inclination from pelagic interbeds with interpreted chron boundaries are shown in Figure 14 (80–200 mbsf), and the locations of the various chron boundaries are continued in Table 4. The intensity and the susceptibility results from MST measurements are shown in Figure 15 (80–200 mbsf).

The RCB cores from Hole 954B provided some intervals of magnetic record that could be placed in their magnetostratigraphic setting with the aid of the paleontological markers, but it was not possible to determine a reliable continuous magnetostratigraphy for the drilled interval. The shallowest part of the record is a short interval of mixed polarity, lying on top of a prolonged normal interval. The top of the nannofossil Subzone CN12c falls in a reversed zone, while the top of CN12b is immediately above the long normal interval. The normal interval is therefore interpreted as the top of C2An (Gauss). At the bottom of this recovered interval there is a transition from normal to reversed polarity in Core 157-954B-8R at approximately 150 mbsf. An age of 3 Ma can be assigned to the core catcher of Core 157-954B-8R because it contains the last appearance of *Gl. margarita.* We therefore provisionally interpret this reversal as the top of C2An.1r (Kaena).

Between 150 and 270 mbsf, no reliable paleomagnetic record was recovered, but a prominent reversed interval was found from 280 to 300 mbsf. This falls in nannofossil Subzone CN9b, below the foraminiferal M13/M12 boundary and so appears to be C3Ar. The top of C3Ar lies in Core 157-954B-21R, but slumps in the critical interval permit us to give only an extended range of between 275 and 281 mbsf. Below C3Ar, between Core 157-954B-23R-5 and 157-954B-24R-1, there is a short normal interval that we interpret as the C3Bn.

Below C3Bn, no reliable magnetostratigraphy is evident until the reversed interval of the C4r from 352 to 371 mbsf. The short normal polarity event in the C4r, the C4r.1n, seems to be as well established as in Hole 953C. The polarity change at the top of the C4An is well recorded in Section 157-954B-31R-1. But only the first parts of the C4An remained. The earlier reversed polarity, the C4Ar, is not recorded. Instead of this a long prominent normal polarity, the C5n, is established. It appears that the short normal and reversed couplets at the end and the beginning of C5n may also be present between 374 and 376 mbsf at the top and between 400 and 425 mbsf at the onset respectively. The couplet at the top is included in C5n, giving the top in Section 157-954B-31R-5. The short reversed interval of the couplet at the base defines the onset of the C5n in the interval from Section 157-954B-34R-2 to 157-954B-34R-3, but we are unable to determine this more precisely, because of major changes in lithology below 406 mbsf (upper part of lithologic Unit IV).

The NRM intensity and susceptibility plots for Holes 954A and 954B (Fig. 15) are again a good proxy for volcanic input as they were in Site 953. The change from lithologic Unit III to IV is recorded be-

Table 4. Polarity chrons: ages and correlated core intervals.

Hole	Name	Age (Ma)	Top Core, section (cm)	Top Depth (mbsf)	Bottom Core, section (cm)	Bottom Depth (mbsf)	Comments
954A							
C1n (o)	Brunhes/Matuyama	0.78	7H-2, 55	50.5	7H-2, 105	51.0	
954B							
C2An (t)	Gauss (t)	2.60	4R-2, 110	112.0	5R-1, 0	120.0	
C3A.n2 (o)		6.56	21R	275.0	21R-5, 115	280.5	
C3Bn (t)		6.92	23R-5, 25	298.5	23R-5, 75	299.5	
C3Bn (o)		7.07	24R-1, 15	302.0	24R-1, 55	303.0	
C4n.2n (t)		7.62	27R-5, 85	338.0	27R-5, 125	339.0	
C4n.2n (o)		8.03	29R-2, 25	352.0	29R-2, 55	353.0	
C4r.1n (t)		8.17	29R-3, 15	353.5	29R-3, 65	354.0	
C4r.1n (o)		8.21	29R-4, 10	354.5	29R-4, 45	355.0	
C4An (t)		8.63	31R-1, 65	370.0	31R-2, 15	371.5	C4Ar missing due to hiatus
C5n.1n (t)		9.64	31R-4, 65	374.5	31R-5, 105	376.5	

Notes: (o) = onset, (t) = top.

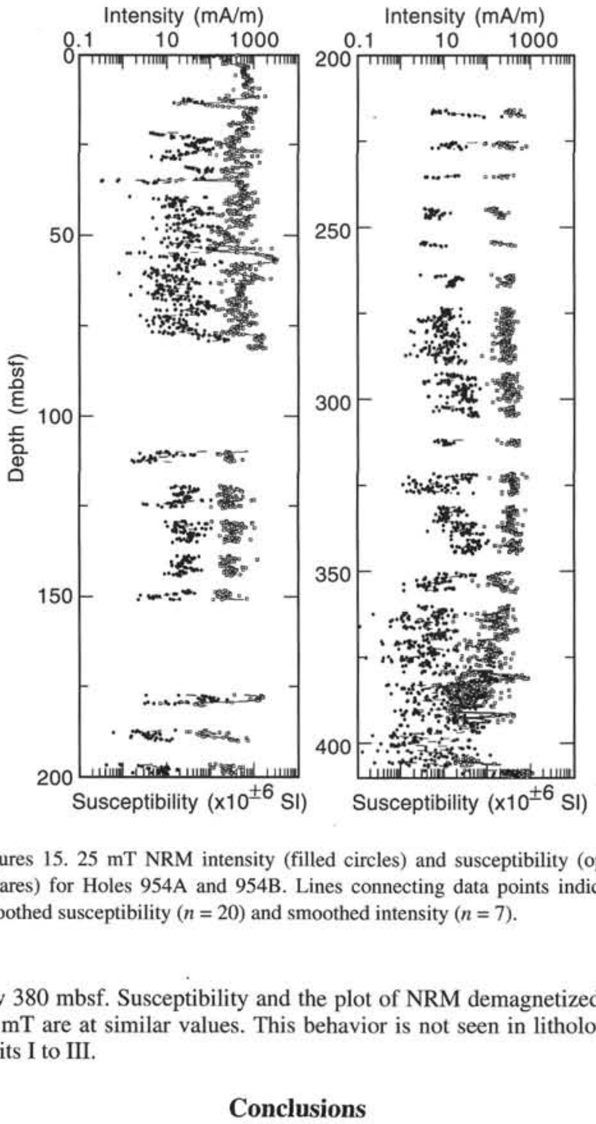

Figures 15. 25 mT NRM intensity (filled circles) and susceptibility (open squares) for Holes 954A and 954B. Lines connecting data points indicate smoothed susceptibility (n = 20) and smoothed intensity (n = 7).

low 380 mbsf. Susceptibility and the plot of NRM demagnetized at 25 mT are at similar values. This behavior is not seen in lithologic Units I to III.

Conclusions

A preliminary magnetostratigraphy for Holes 954A and 954B has been developed that is consistent with the biostratigraphy, which has again been used to constrain the magnetostratigraphy. The missing C4Ar reversed polarity chron leads us to the conclusion that there is a major hiatus in the sediment record (see "Biostratigraphy," this chapter) lasting for more than 0.7 to less than 1.0 m.y. for this event.

PETROGRAPHY, MINERALOGY, AND GEOCHEMISTRY OF VOLCANICLASTIC SEDIMENTS

A variety of volcaniclastic sediments were recovered at Site 954, including fine-grained ash-fall layers, crystal-lithic silts and sands with biogenic fragments, pumiceous sands, lapillistones, and volcanic breccias (Table 5). As at Site 953, the stratigraphic succession of lithics, crystals, and trace element geochemistry of whole-rock and sediment samples closely parallels the subaerial volcanic stratigraphy of Gran Canaria (Schmincke, 1994), with the exception that deposits contemporaneous with the Fataga and Mogan volcanic intervals are absent.

Petrography and Mineralogy

Unit I (0–177 mbsf) contains numerous beds of crystal-lithic silt and sand, with variable proportions of biogenic material and minor pumiceous sands, vitric ash, and lapillistone. Dominant lithic clasts in Unit I are trachyphonolitic lava (with aegirine in the groundmass) and tuff (pumice and welded tuff), and minor basalt (tachylitic plagioclase-phyric basalt and fresh sideromelane). One clast of hauyne-bearing, aegirine-augite-phyric phonolite occurs in interval 157-954A-2H-4, 84–86 cm (Fig. 16). Rare basanite, phonolite, and olivine nephelinite clasts occur at the top of the unit. Crystals comprise alkali feldspar, brown amphibole, Ti-augite, and aegirine-augite. Pumice sand is present in Core 157-954B-4R and consists of alkali feldspar-phyric pumice, glass shards, and crystals of alkali feldspar and minor clinopyroxene (Ti-augite > aegirine-augite), together with minor tachylitic and plagioclase-phyric basaltic fragments. The lapillistone (Core 157-954B-1R) contains lapilli-size angular basaltic and trachyphonolitic fragments with crystals of alkali feldspar and Ti-augite. Vitric ash layers consist of unaltered, colorless felsic glass shards with abundant microlites (Sample 157-954A-2H-CC, 13–15 cm). The ash layers are most likely the result of fallout from explosive volcanic activity on Tenerife. The main sources of volcaniclastic lithics and crystals are the volcanic formations of the Miocene Fataga group (trachyphonolite), the Pliocene Roque Nublo Group (Ti-augite, brown amphibole, hauyne-bearing rocks), and late Pliocene to Holocene post-Roque Nublo basalts and basanites (sideromelane, basaltic lithics).

Unit II (177–179 mbsf) is composed entirely of lapillistone (Fig. 17). Phonolitic and basaltic fragments, some of which are tachylitic, dominate in this unit with minor sideromelane shards and pumice. Altered alkali feldspars are present in the matrix. In the basaltic clasts, crystals are euhedral clinopyroxene (Ti-augite) and plagioclase microlites. The matrix is calcareous with a zeolitic cement in pore spaces. The lapillistone of Unit II, which was emplaced during the Roque Nublo Group time interval, probably corresponds to reworked volcaniclastic material of this group.

Unit III (179–408 mbsf) contains thin interbeds of crystal-lithic silt and sand. Minor volcaniclastic grains and crystals are commonly dispersed within mixed sedimentary rocks (Fig. 18). Volcanic grains are mainly felsic rock fragments (trachyphonolitic lava). Basaltic tachylitic fragments are less abundant. Minor crystals include alkali feldspar, biotite, alkali amphibole (Mogan Group), clinopyroxene (Ti-augite and rare aegirine), and plagioclase. Minor felsic glass shards and pumice are scattered within the matrix of mixed sedimentary rocks. Unit III is contemporaneous with the late Miocene to Pliocene volcanic hiatus on Gran Canaria. Only minor mafic (basalt and sideromelane) and felsic (trachyphonolite) volcaniclastic material is found in this interval and the main source was erosion of volcanic rocks from the Fataga Group, with some input from Mogan Group rocks.

Unit IV (408–446 mbsf) is represented by basaltic breccia. Large clasts are altered alkali basalts mostly with tachylitic texture. Minerals are olivine pseudomorphs replaced by a carbonate-zeolite mixture and large phenocrysts or minor glomerocrysts of Ti-augite (Fig. 19). The groundmass contains microlites of Ti-augite, plagioclase, quenched-textured oxides and secondary minerals (zeolites, carbonates). Many vesicles are filled with zeolites and carbonates. The petrographic and chemical composition of the basaltic fragments of the breccia indicate they are correlative to the shield stage of Gran Canaria (15 Ma).

Geochemistry

Samples of vitric crystal ash, calcareous sand with lithics, polymict lapillistone, dark gray claystone, and basaltic breccia from Units I, II, III, and IV were analyzed by XRF using analytical conditions discussed in the "Explanatory Notes" (this volume). The concentrations of selected trace elements for nine samples are presented in Table 6 and Figures 20 and 21.

A sample of vitric crystal ash from Unit I has high contents of Zr and Nb indicating an evolved composition. A polymict lapillistone from Unit II has a Zr/Nb ratio of 3.6, very similar to the ratio for magmas erupted during the Roque Nublo stage of volcanism on Gran Canaria (Schmincke, 1982). The unit is late Pliocene in age and thus coincides with this period of volcanism. A dark gray claystone from Unit III has a similar Zr/Nb ratio, 3.8, but has higher absolute abundances of incompatible elements such as Zr, Nb, Ce, and very low contents of Ni, Cr, and V (Table 6, Fig. 21). This suggests that the layer was derived from the erosion of more evolved magmas, probably from the Fataga stage volcanism on Gran Canaria (9.5–13.4 Ma).

The mafic composition of five samples of basaltic breccia from Unit IV is reflected in the high Ni, Cr, and V contents (Table 6, Fig. 21). The Zr/Nb ratios range from 5.7 to 11.0.

INORGANIC GEOCHEMISTRY

Introduction and Operation

A total of 22 interstitial-water samples were taken between 11.95 and 404.00 mbsf at Site 954 (Table 7). The sampling strategy and analytical methods followed those employed at Sites 950–953. Samples were analyzed for pH, salinity, chlorinity, alkalinity, sulfate, ammonia, sodium, potassium, lithium, silica, calcium, magnesium, and strontium (see "Explanatory Notes," this volume).

The uppermost 100 m at Site 954 display small changes in pore-water composition which are being driven by the bacterially mediated oxidation of organic matter. By contrast, extreme pore-water variation is seen immediately above and below the lapillistone of lithostratigraphic Unit II (see "Lithostratigraphy," this chapter) around 180 mbsf, and below 300 mbsf approaching the boundary between nannofossil chalk Unit III and the underlying basaltic breccia Unit IV. Large increases in alkalinity, salinity, sodium, lithium, silica, magnesium, and calcium, with slightly depleted chlorinity and sulfate here are associated with CO_2-charged effervescent pore waters.

Sulfate, Ammonia, and Alkalinity

Sulfate (Fig. 22) contents are around 28.5 mmol/L, in the upper 80 m, only very slightly depleted compared to seawater values (28.9 mmol/L). Marginally higher concentrations of around 30.5 mmol/L characterize the interval around 100–150 mbsf, at the base of lithostratigraphic Unit I (see "Biostratigraphy," this chapter). Sulfate is depleted at 25.4 mmol/L in the chalks immediately below lapillistone Unit II (179 mbsf), rises back to seawater values below this at 200 mbsf, and then declines again to 25–26 mmol/L through the bulk of Unit III. The low gradients in the profile indicate very low rates of sulfate reduction at Site 954, a consequence of the low organic matter content (typically <0.2%; see "Organic Geochemistry," this chapter).

Alkalinity decreases from 3.2 mmol/L at 12 mbsf (significantly higher than the 2.3 mmol/L of seawater), to a minimum of 1.7 mmol/L around 65 mbsf (Fig. 22) before increasing to an unusually high maximum of 118 mmol/L in the chalks at the top of Unit II at 179 mbsf. Below this, alkalinity again decreases rapidly to around 1.2 mmol/L between 145 and 300 mbsf, producing a symmetrical peak centered on lapillistone Unit II. From 300 mbsf, a further rapid rise peaks in concentrations of ~100 mmol/L in the 50 m of chalks immediately overlying the basaltic breccia Unit IV at 408 mbsf.

Alkalinities higher than those of seawater in surficial sediments may be attributed to bacterial processes, as indicated by elevated ammonia concentrations in this interval (Fig. 22), but the much larger maxima deeper in the section must have a different origin. They may result from the introduction of gaseous CO_2 or CO_2-charged pore fluids, related to Holocene volcanism in northern Gran Canaria (Schmincke, 1982). However, the mode of such introduction is unclear. Both the lapillistone unit, the apparent focus of the upper maximum, and the basaltic breccia at the base of the sequence have low porosities and high bulk densities (see "Physical Properties," this chapter), which almost certainly equate to low permeabilities, so they are unlikely to act as fluid conduits. Sands in unrecovered intervals around 180 mbsf might serve this purpose in the upper section, but no such lithologies were noted in the well-recovered basal sequence. The relationship between the high alkalinity zones and alteration processes also remains unclear.

Ammonia concentrations are low in the interstitial waters at Site 954 as would be predicted by the absence of significant sulfate depletion; NH_4^+ attains a maximum of around 340 µmol/L at 26 mbsf (Fig. 22) and then decreases to a minimum of ~140 µmol/L at 180 mbsf. Concentrations rise again to ~200 µmol/L between 220–340 mbsf and then decline to a minimum of 70 µmol/L at the base of Unit II. These trends are consistent with organic matter degradation generating NH_4^+ in the uppermost beds, with uptake of ammonia by diagenetic clay minerals taking place in volcaniclastic-rich Units II and IV. The lack of significant sulfate depletion within the ammonia maximum indicates very low rates of sulfate reduction, enabling downward diffusion of seawater sulfate to keep pace with bacterial sulfate-reduction rates. Higher than seawater concentrations of sulfate in the ammonia-depleted pore waters below imply a modest input of sediment-derived sulfate. The large alkalinity maxima are both ammonia and sulfate depleted.

Table 5. Summary of volcaniclastic components, Site 954.

Unit	Subunit	Core (top)	Depth (mbsf)	Age (Ma)	Period	Lithologies with volcanic components
I		1H	0.0	0.0	Post-Roque Nublo	Calcareous-lithic-crystal silt and sand, pumice sand, lapillistone Volcanic ash
II		11R-1	177	2.8	Roque Nublo	Lapillistone
III		11R-2	179	2.8	Volcanic hiatus	Crystal-lithic silt and sand
IV		35R	408	14?	Shield	Basaltic breccia

Figure 16. Photomicrograph of a hauyne-bearing, aegirine-augite-phyric phonolitic clast. Hauyne corresponds to the colorless hexagonal mineral sections. Field of view is 2.0 mm wide. Sample 157-954A-2H-4, 84–86 cm, plane polarized light.

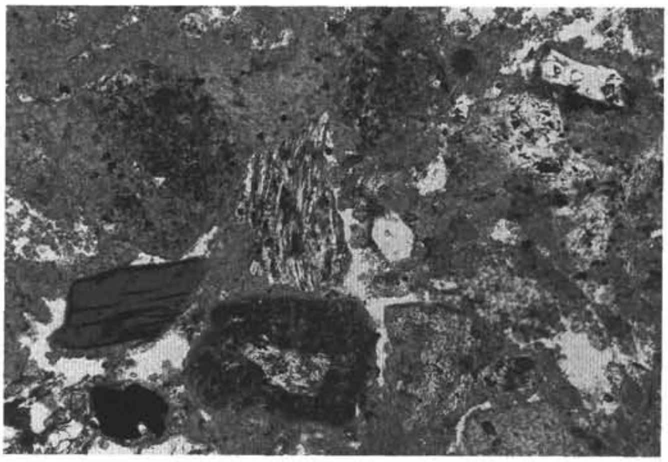

Figure 18. Photomicrograph of a mixed sedimentary rock of Unit III. Note the subrounded trachyphonolitic and basaltic clasts, and the amphibole crystal within the calcareous matrix. Field of view is 2.0 mm wide. Sample 157-954B-27R-5, 13–14 cm, plane polarized light.

Figure 17. Photomicrograph of the lapillistone of Unit II. Note the subrounded volcanic clasts and the clinopyroxene crystal within the fine-grained calcareous matrix. Field of view is 8.0 mm wide. Sample 157-954B-1R-1, 34–39 cm, plane polarized light.

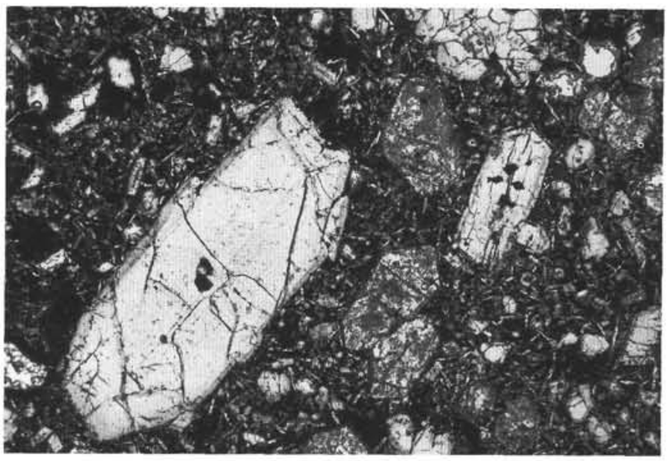

Figure 19. Photomicrograph of an altered alkali basalt from the basaltic breccia of Unit IV. Note the clinopyroxene (Ti augite) phenocrysts and olivine pseudomorphs. Field of view is 8.0 mm wide. Sample 157-954B-35R-2, 7–11 cm, plane polarized light.

Table 5 (continued).

Unit	Volcanic components: Rock fragments	Crystals	Vitric clasts
I	Basalt (tachylite > crystalline) trachyphonolite lava and tuff	Plagioclase, clinopyroxene > brown amphibole > biotite rare hauyne	Pumice, sideromelane
		Minor clinopyroxene > biotite, plagioclase	Glass shards
II	Basalt (tachylite, crystalline) trachyphonolite lava and tuff	Plagioclase,Ti-augite > alkaline feldspar	Minor sideromelane, pumice
III	Trachyphonolite lava and tuff basalt (tachylite)	Alkaline feldspar > clinopyroxene, biotite, alkaline amphibole, plagioclase	Very minor glass shards and pumice
IV	Alkali basalt (mostly tachylite)	Ti-augite > olivine pseudomorphs > plagioclase >opaques	Minor sideromelane

Table 6. XRF major and trace element analyses of whole-rock samples, Site 954.

Hole, core, section:	954A-3H-1	954A-7H-6	954B-11R-1	954B-28R-2	954B-35R-2	954B-36R-1	954B-37R-1	954B-38R-1	954B-39R-3
Interval (cm):	98–101	83–87	91–93	36–38	7–11	7–12	137–140	5–16	24–28
Depth (mbsf):	11.48	56.83	178.11	342.51	409.37	417.37	428.17	436.45	444.27
Lithologic unit:	I	I	II	III	IV	IV	IV	IV	IV
Major elements (wt%)									
SiO_2	55.26	46.22	45.18		46.31	47.13	47.41	44.51	41.59
TiO_2	1.33	3.74	3.51		3.40	4.90	4.54	5.62	4.15
Al_2O_3	14.97	13.82	12.74		10.24	12.17	11.60	10.94	9.03
Fe_2O_3	7.96	13.49	13.01		12.14	11.45	12.55	14.54	16.75
MnO	0.33	0.18	0.16		0.16	0.18	0.26	0.18	0.24
MgO	3.84	7.35	6.94		9.81	6.76	8.86	8.86	11.43
CaO	3.83	9.81	12.15		14.54	12.60	10.57	10.75	13.40
Na_2O	5.76	2.93	2.71		1.95	2.35	2.32	2.17	1.51
K_2O	3.52	1.53	1.39		0.65	1.57	0.96	1.38	1.01
P_2O_5	0.80	0.58	0.58		0.37	0.69	0.48	0.77	0.40
Total	97.60	99.65	98.37		99.57	99.80	99.55	99.72	99.50
LOI	3.65	1.01	8.40		8.17	2.30	2.21	1.46	13.43
Trace elements (ppm)									
Cr	64	222	253	13	1696	205	665	320	1144
Ni	55	112	129	11	334	113	247	178	303
Cu	28	69	101	10	127	253	91	69	103
V	70	277	267	53	279	386	365	356	304
Zn	265	125	109	184	108	140	137	118	121
Sr	2870	847	1215	815	488	759	515	582	339
Ba	1525	492	364	937	162	308	121	187	79
Rb	69	26	18	86	9	28	14	16	13
Y	66	27	24	29	23	32	32	34	26
Zr	1947	363	261	864	270	421	423	474	355
Nb	354	81	73	225	39	74	52	58	32
Ce	495	101	91	307	68	119	111	106	67
Zr/Nb	5.5	4.5	3.6	3.8	7.0	5.7	8.1	8.2	11.0

Salinity and Chloride

Salinities (Fig. 23) lie between 35 and 36 g/kg except within the two alkalinity maxima around 180 mbsf and below 300 mbsf, where salinities increase considerably. A maximum of 44 g/kg is attained in the upper maximum, immediately below Unit II.

Chloride (Fig. 23) shows two opposing trends: as at Site 953, there is broad increase with depth, from a seawater-like value of 561 mmol/L at 12 mbsf, to a maximum of 581 mmol/L at 300 mbsf. However, superimposed on this trend are two chlorinity minima associated with the alkalinity and salinity maxima. In contrast to Site 953, therefore, salinity and chlorinity display opposing trends around the volcaniclastic units.

Sodium, Potassium, and Lithium

Pore-water potassium concentrations (Fig. 24) decline markedly from 10.6–5.6 mmol/L between 12 and 150 mbsf. Below this, potassium levels remain low except in the alkalinity maxima where levels rise back to seawater-like concentrations. Declining potassium is attributed to the precipitation of phillipsite, while the potassium maxima are most likely caused by the liberation of alkalis from altered volcanic glasses within Units II and IV.

Sodium is variable but broadly increases from seawater compositions of 480 mmol/L at the top of the hole to a maximum of 600 mmol/L at 280 mbsf before declining again to around 550 mmol/L near the bottom of the section. No significant change in sodium concentration occurs around the upper alkalinity maximum. The modest increase in pore-water sodium may be derived from the breakdown of sodic glasses; declining sodium concentrations toward Unit VI indicate uptake by alteration products within the basaltic breccias.

Lithium (Fig. 24) occurs at 21–25 µmol/L in the upper 130 m, but increases to high concentrations of >250 µmol/L in the upper alkalinity maximum. Concentrations fall back to slightly higher than seawater values below, but they rise again to a second >250 µmol/L peak at the base of the section. High concentrations of lithium in pore waters might be attributed to the breakdown of K-, Li-rich volcanic glasses by CO_2-charged pore waters and/or the introduction of externally derived alkali metal-rich fluids.

Silica

Silica displays a similar trend to many other constituents (Fig. 25), occurring at variable low concentrations (100–400 µmol/L) through much of the succession, but attaining very high concentrations of 1200 and 1500 µmol/L within the upper and at the base of the

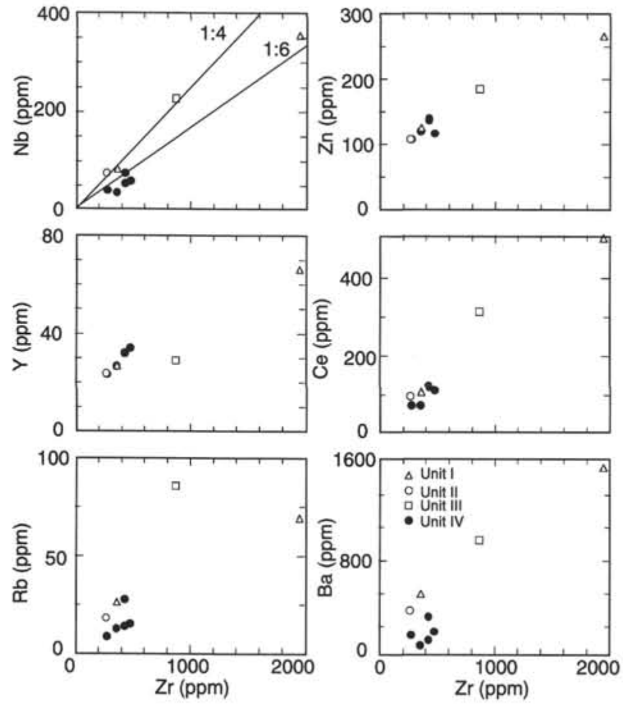

Figure 20. Plots of Nb, Zn, Y, Ce, Rb, and Ba vs. Zr for samples from Units I, II, III, and IV at Site 954.

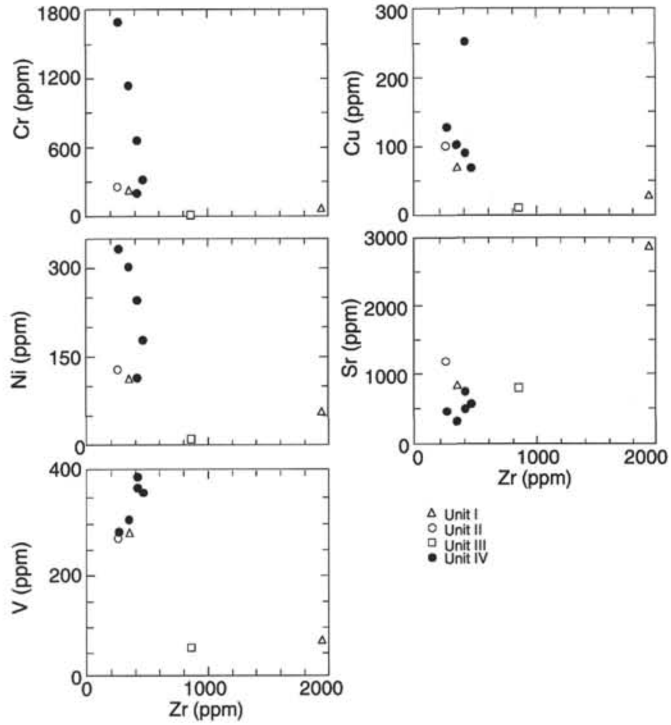

Figure 21. Plots of Cr, Cu, Ni, Sr, and V vs. Zr for samples from Units I, II, III, and IV at Site 954.

Table 7. Interstitial-water geochemistry, Holes 954A and 954B.

Core, section, interval (cm)	Depth (mbsf)	pH	Salinity (g/kg)	Cl (mmol/L)	Alkalinity (mmol/L)	SO_4 (mmol/L)	NH_4 (μmol/L)	Na (mmol/L)	K (mmol/L)	Li (μmol/L)	SiO_2 (μmol/L)	Ca (mmol/L)	Mg (mmol/L)	Sr (μmol/L)	Mg/Ca (molar ratio)	Sr/Ca (molar ratio)
157-954A-																
3H-1, 145–150	11.95	7.50	36.0	561	3.22	28.5	242	480	10.6	21	376	7.49	52.8	243	7.05	0.032
4H-4R, 145–150	25.95	7.44	35.5	567	2.75	28.7	337	515	10.4	25	405	7.60	51.9	400	6.83	0.053
5H-3R, 145–150	33.95	7.52	35.5	567	2.33	28.4	321	.539	9.19	24	221	9.04	52.3	449	5.79	0.050
6H-5R, 145–150	46.45	7.60	36.0	566	2.15	29.5	310	496	8.77	24	409	9.68	49.3	497	5.09	0.051
7H-3R, 145–150	52.95	7.63	35.5	567	1.92	28.1	274	510	8.03	22	244	9.07	47.6	439	5.25	0.048
8H-5R, 145–150	65.45	7.40	35.5	568	1.72	28.6	311	500	8.30	25	380	11.6	46.9	494	4.04	0.043
10H-1R, 145–150	78.45	7.77	36.0	570	1.83	28.7	214	559	8.30	25	167	11.1	46.1	463	4.15	0.042
157-954B-																
4R-1R, 140–150	111.10	7.70	36.0	565	2.61	30.5	185	534	6.59	21	403	9.52	49.9	330	5.24	0.035
6R-3R, 140–150	133.40	7.65	36.0	569	15.2	30.4	172	547	5.89	22	269	2.62	62.6	123	23.9	0.047
8R-1R, 120–130	149.40	7.65	40.0	570	57.3	30.3	187	504	5.57	64	869	4.74	81.8	216	17.3	0.046
11R-2R, 63–73	179.20	7.57	44.0	561	118	25.4	142	556	9.93	259	1200	18.3	95.2	112	5.21	0.006
13R-1R, 140–150	197.90	7.47	40.5	576	75.2	28.9	175	564	5.68	128	967	8.52	79.9	453	9.38	0.053
15R-1R, 105–115	216.75	7.66	36.0	575	9.50	26.7	207	574	5.58	35	267	3.09	41.7	374	13.5	0.121
18R-1R, 140–150	245.80	7.65	36.0	576	1.26	25.1	212	530	5.43	29	116	9.88	30.1	373	3.05	0.038
21R-5R, 140–150	280.70	7.89	36.0	578	1.21	25.3	187	603	5.89	31	127	7.16	30.2	276	4.22	0.039
24R-1R, 133–148	303.33	8.22	36.0	581	1.06	25.7	203	591	6.15	30	131	5.70	31.3	224	5.49	0.039
27R-3R, 140–150	335.50	7.91	36.5	570	20.0	25.9	170	580	5.90	77	599	4.23	40.9	200	9.67	0.047
30R-5R, 131–141	366.55	7.57	41.5	562	93.7	26.2	132	516	8.68	247	1050	11.3	73.5	178	6.50	0.016
31R-5R, 130–140	376.54	7.75	42.0	563	95.3	26.9	116	571	8.83	257	1120	11.5	76.2	156	6.63	0.014
32R-4R, 136–146	384.57	7.72	42.0	557	105	26.2	107	530	9.30	272	1110	12.9	77.6	132	6.02	0.010
33R-4R, 140–150	394.40	7.68	42.5	559	102	24.7	89.9	525	10.5	274	1380	11.9	78.0	106	6.55	0.009
34R-4R, 140–150	404.00	7.82	42.0	559	103	26.2	71.2	551	10.8	261	1470	15.0	82.6	88	5.51	0.006

lower alkalinity maxima. Pore-water silica concentrations at this site, therefore, seem to demonstrate an overriding control by diagenetic processes accompanying the dissolution of volcanic glasses.

Magnesium, Calcium, and Strontium

Like many other pore-water constituents at Site 954, high concentrations of Mg^{2+} of up to 95 and 83 mmol/L (Fig. 26) associated with the upper and lower alkalinity maxima are superimposed on a background trend of declining concentrations, from near-seawater concentrations of 53 mmol/L at the top to 30 mmol/L in the lower part of the sequence.

Calcium displays an unusually complex distribution (Fig. 26), with depleted values of 7.5 mmol/L at 12 mbsf indicating early diagenetic Ca^{2+} uptake into the solid phase in surficial sediments. Below this, concentrations rise again to 11.6 mmol/L at 65 mbsf, before decreasing sharply below, producing a minimum of 2.6 mmol/L at 130 mbsf. A Ca^{2+} high of 18 mmol/L at the alkalinity maximum is underlain by a further low of 3.1 mmol/L calcium at 215 mbsf, followed by a minor peak and then decline down to 335 mbsf before steadily rising again to 15 mmol/L at the Unit III/IV boundary.

The regular nature of the Ca minima, which form a symmetrical pair on either side of lapillistone Unit II and occur in the lower part of Unit III some distance above basaltic breccia Unit IV, strongly

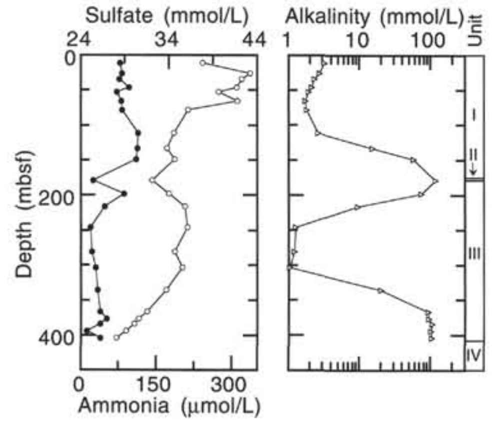

Figure 22. Interstitial-water sulfate (filled circles), ammonia (open circles), and alkalinity at Site 954. Lithostratigraphic units indicated by roman numerals.

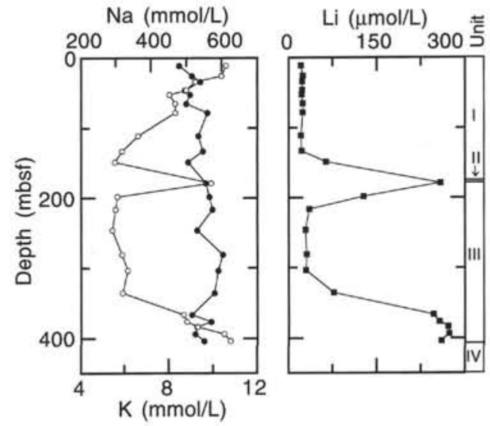

Figure 24. Interstitial-water sodium (filled circles), potassium (open circles), and lithium at Site 954. Lithostratigraphic units indicated by roman numerals.

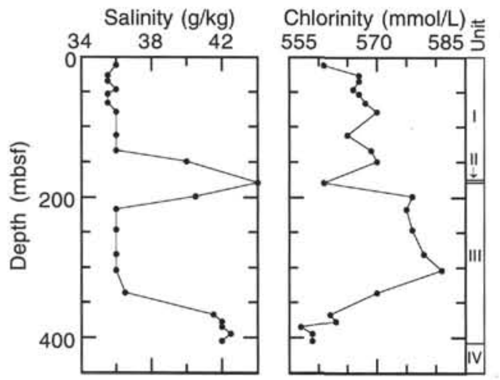

Figure 23. Interstitial-water salinity and chlorinity at Site 954. Lithostratigraphic units indicated by roman numerals.

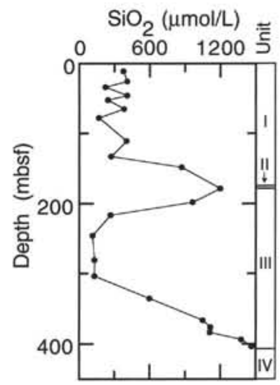

Figure 25. Interstitial-water silica at Site 954. Lithostratigraphic units indicated by roman numerals.

suggest that Ca is being supplied to solution by dissolution of glasses in the volcaniclastic breccias, and is then being incorporated into a diagenetic phase within the intervening sediments. It is noteworthy, therefore, that dolostone intervals were observed around the uppermost and lowest of the three Ca^{2+} minima. Magnesium shows no significant depletion at these levels (Fig. 26), but this may be because the higher levels of pore-water Mg^{2+} available are less sensitive to dolomite precipitation than Ca^{2+}, which occurs at up to one order of magnitude lower concentrations. Mg/Ca ratios display complex trends (Fig. 26), but three peaks coincide with the three calcium minima, which we tentatively attribute to sites of active dolomite precipitation.

Strontium concentrations rise from 243 µmol/L at 12 mbsf to ~500 µmol/L at 45–65 mbsf, decline again to 100–200 µmol/L between 130 and 180 mbsf, rise to a second peak of 450 µmol/L in the upper part of Unit III at 200 mbsf, and then decline gradually below that to <90 µmol/L at the bottom of the unit. These trends indicate that unlike the other two alkali earths, Sr is being incorporated into, rather than supplied by, the volcaniclastic levels in the sequence. As at Site 953, Mg/Ca and Sr/Ca ratios display similar trends (Fig. 26) which are essentially mirror images of the Ca^{2+} profile.

Interpretation of trends in pore-water calcium, magnesium, and strontium must be treated with caution. It is unlikely that either the calcium or alkalinity data are fully quantitative at Site 954. Appreciable CO_2-degassing, caused by increasing temperature and declining pressure, was observed in the high-alkalinity intervals after the core was brought to the surface, and effervescence continued during and after the squeezing operation. Such degassing would be expected to cause the precipitation of carbonate, and indeed shipboard pore-water samples from these intervals displayed significant precipitates after a few days. Shore-based studies of acidified pore waters will allow better assessment of the shipboard data, but only in-situ measurements could be fully quantitative.

Conclusions

Site 954 is unusual in that large increases in alkalinity, salinity, sodium, lithium, silica, magnesium, and calcium, and slightly depleted chlorinity and sulfate, are associated with CO_2-charged effervescent pore waters that lack evidence of significant organic-matter driven diagenesis. Alkalinities of up to 120 mmol/L are recorded with more than 250 µmol/L Li and 1500 µmol/L SiO_2. Such extreme compositions are highly atypical of oceanic pore waters, and it is speculated that they result from a combination of diagenetic processes affecting basaltic-phonolitic glasses in the volcaniclastic units and the introduction of CO_2^- (and possibly alkali metal) charged fluids from recent volcanic activity in the area.

ORGANIC GEOCHEMISTRY

The shipboard organic geochemistry program at Site 954 followed the same procedures used for Sites 950–953.

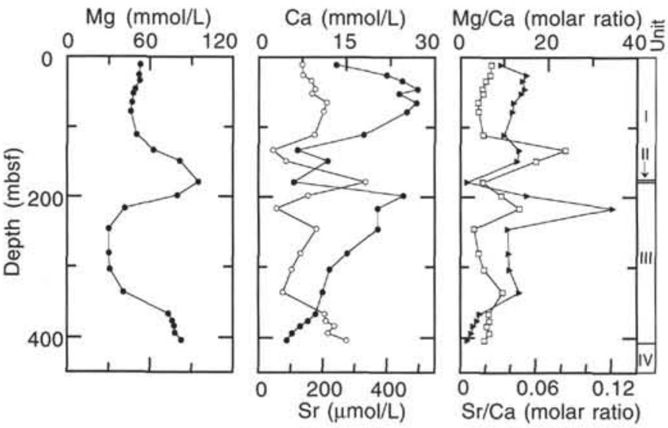

Figure 26. Interstitial-water magnesium, calcium (open circles), strontium (filled circles), and Mg/Ca (open squares) and Sr/Ca (filled triangles) ratios at Site 954.

Volatile Hydrocarbons

Concentrations of methane (C_1) and ethane (C_2) gases were monitored in every core by the standard ODP headspace-sampling technique as part of the SSP program. The methane content remained constantly low throughout the entire lithological sequence of Site 954, varying between 2 and 6 ppmv. No ethane was detected.

Carbon, Nitrogen, and Sulfur Concentrations

A total of 122 analyses of carbonate were made related to the lithology as for Sites 950–953. A number of samples were then selected for analyses of organic carbon, nitrogen, and sulfur. A total of 32 samples were run on the CNS instrument. Organic carbon contents were uniformly low, ranging from below detection to 0.22%, with only nine values above 0.10%. Nitrogen varied between below detection to 0.02%. Sulfur concentrations varied from below detection to 4.0%, with only three samples above 0.5%. No trends were observed in the C, N, and S data and values were too small to give any meaningful correlation.

PHYSICAL PROPERTIES

Introduction

The shipboard physical properties measurements program at Site 954 included nondestructive measurements of bulk density, bulk magnetic susceptibility, *P*-wave velocity, and total natural gamma activity using the MST, as well as thermal conductivity on whole sections of core. Discrete measurements were also made of velocity, shear strength, and index properties. Sample intervals for the discrete measurements were selected from the most undisturbed sections of the working half of the core.

Whole-core Measurements

MST

Whole-round measurements of GRAPE density, magnetic susceptibility, *P*-wave velocity, and natural gamma activity were made on all cores throughout Hole 954A except the two XCB cores, 11X and 12X. For Hole 954B all properties were measured except *P*-wave velocity. Filtered and raw MST are shown in Figures 27 through 38. GRAPE density, magnetic susceptibility, and *P*-wave velocity were filtered with a 12.5 cm running median filter. The natural gamma data, because of less frequent sampling, was filtered with a 100.0 cm running median. All data points falling within the bounds of the plot are shown by crosses on Figures 27 through 29 for Hole 954A and Figures 33 through 35 for Hole 954B. The filtered data are indicated by the thin black line. Data gaps longer than the filter length are indicated by discontinuities in the line.

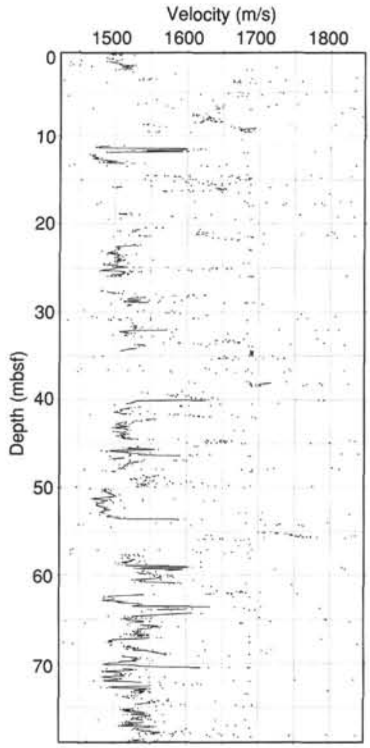

Figure 27. MST velocity, Hole 954A. Filtered data indicated by lines, raw data by discrete points.

The quality of the velocity determination can be tied to the signal level parameter recorded in the data file. This parameter is scaled to the amplitude of the received signal: higher values indicate a stronger signal and a better velocity measurement. Figure 39 shows the MST velocity data from Hole 954A plotted against the value of signal level for that determination. The parameter varies between 0 and 255. Data measurements where the signal level fell below 175 and velocities that fell outside the window defined by the mean ±1.5 times the standard deviation of the population of velocities were excluded from Figure 27. Many of the velocity determinations in the upper part of Hole 954A were excluded. The loose sands recovered over this interval did not transmit sound efficiently.

Figures 27 thorough 29 show data from the *P*-wave logger, GRAPE density, and magnetic susceptibility, respectively. All MST data from Hole 954A are plotted in Figure 30. Two-dimensional crossplots of these data are shown in Figure 31. Notice the correlations between density and velocity, and weaker correlation between magnetic susceptibility and density or velocity. For example, the upper-left plot of Figure 31 shows that increases in density follow increases in velocity, whereas increases in velocity or density correspond to only slight increases in magnetic susceptibility. Velocity, density, and magnetic susceptibility are displayed on three-dimensional crossplots in Figure 32. Figures 33 through 35 show Hole 954B GRAPE density, magnetic susceptibility, and natural gamma activity, respectively. The filtered data are shown together in Figures 36 and 37 for ranges 80–280 and 280–445 mbsf, respectively. Crossplots of the Hole 954B data are displayed in Figure 38.

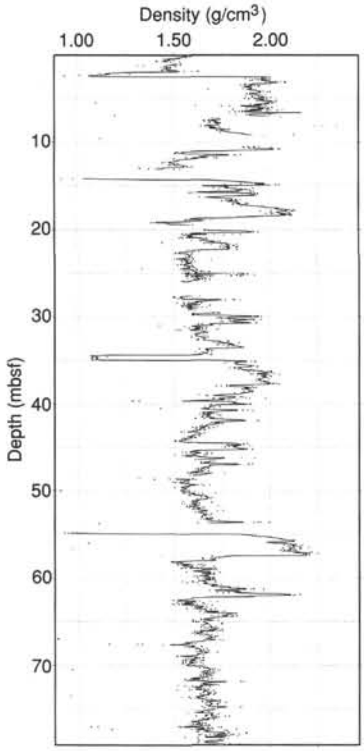

Figure 28. MST density, Hole 954A. Filtered data indicated by lines, raw data by discrete points.

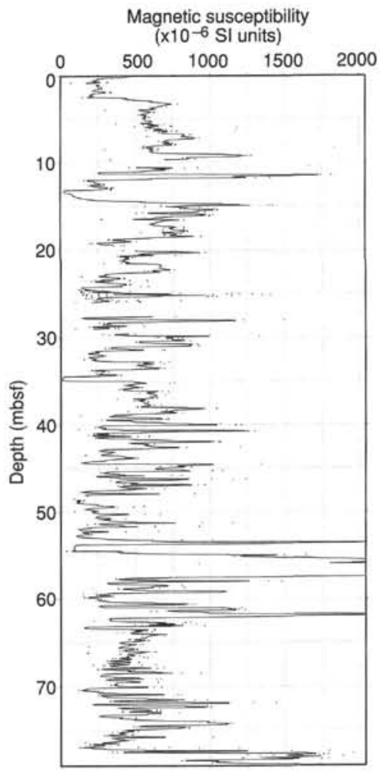

Figure 29. MST magnetic susceptibility, Hole 954A. Filtered data indicated by lines, raw data by discrete points.

Thermal Conductivity

Thermal conductivity measurements were performed on two or three sections of each core. Needles were inserted 50 cm from the top of each measured section on all cores from Hole 954A, from the mud line to a depth of 74 mbsf. The values for the thermal conductivity vary from 0.88 to 1.31 W/(m·K). The data are compiled in Table 8 and shown in Figure 40 together with the porosity, carbonate content, and wet-water content (see "Lithostratigraphy," this chapter). A negative correlation between the thermal conductivity and the porosity and with water content is generally expected. For example, while thermal conductivity values increase, so does the carbonate content, while porosity and water content typically decrease. However, carbonate sampling was not coordinated with discrete index property sampling or with the thermal conductivity measurements.

Split-core Measurements

Velocity

The *P*-wave velocity was measured in Hole 954A with the DSV transducers inserted along the core axis up to Core 157-954A-7H. Beginning with Core 157-954A-8H, the sediments became too lithified to use the DSV. The Hamilton Frame was then used to obtain compressional velocities. Measurements were made with the core in the liner, and typically 1 to 8 values per section were determined. The results from both holes are compiled in Table 9. There is a gradual increase in velocity with depth to about 2 km/s. At 408 mbsf there is an abrupt increase in velocity to an average of 4.74 km/s. This change marks the onset of the volcanic breccia, lithostratigraphic Unit IV. Prior to this unit, there are a few high velocities (some as much as 4 km/s). These zones correspond to the volcanic lapilli and scattered sandy intervals. A plot of all velocity data is shown in Figure 41, alongside bulk density, water content, and porosity. Notice that the high velocities corresponded to highs in density and lows in water content and porosity (see discussion below). Some of the velocities are over 6 km/s, corresponding to measurements of individual basaltic clasts.

Shear Strength

Both the motorized vane shear and the handheld penetrometer were used together to measure the sediment strength to provide a means of comparison between the two instruments. Vane shear measurements were made throughout this hole, beginning with the first core of Hole 954A, and then into Hole 954B as far as Section 157-954B-5R-4 at 124.66 mbsf where the sediments became too stiff for any of the vane springs. Penetrometer measurements were made from 22.40 to 144.30 mbsf where the sediments became too fractured for use of the instrument. Data are presented in Table 10, and plotted against depth in Figure 42 alongside water content, void ratio, and grain density. Notice that the vane shear and penetrometer values correlate well throughout the entire interval in which both measurements were made simultaneously. Penetrometer measurements are generally higher, sometimes by as much as 70 kPa. The data show a general trend of increasing strength downhole to about 85 kPa. However, the data show a wide scatter throughout with variations corresponding to lithologic changes. Limitations in the instrumentation may also account for some of the data scatter.

Index Properties

Index properties were determined by gravimetric methods using discrete samples taken at an average rate of 1 per section in each core throughout Holes 954A and 954B. Calculations of index properties have been made following Methods B and C (see "Explanatory Notes," this volume). Values of the index properties from both meth-

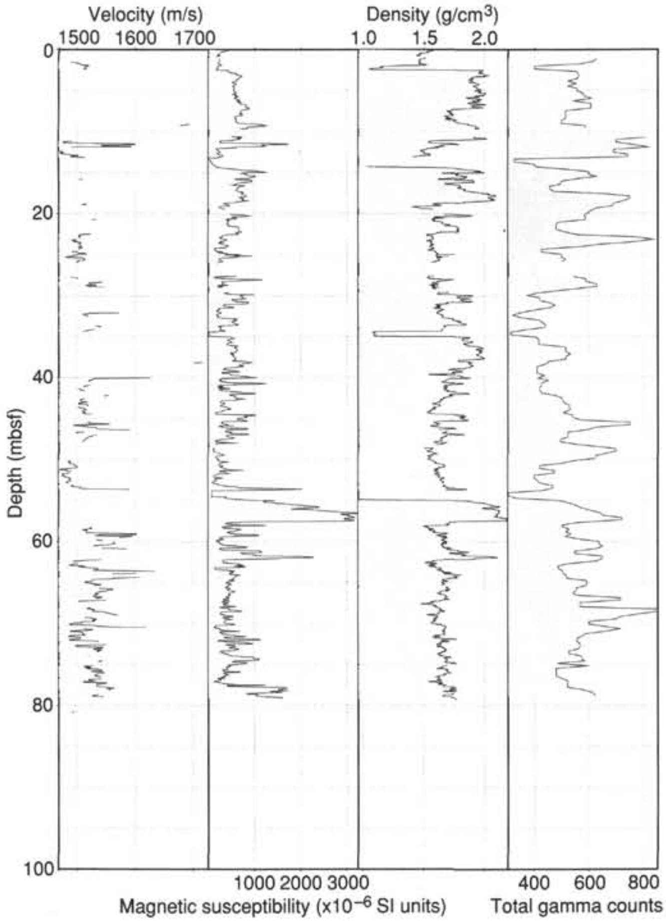

Figure 30. Filtered MST velocity, magnetic susceptibility, gamma-ray density, and total counts for Hole 954A.

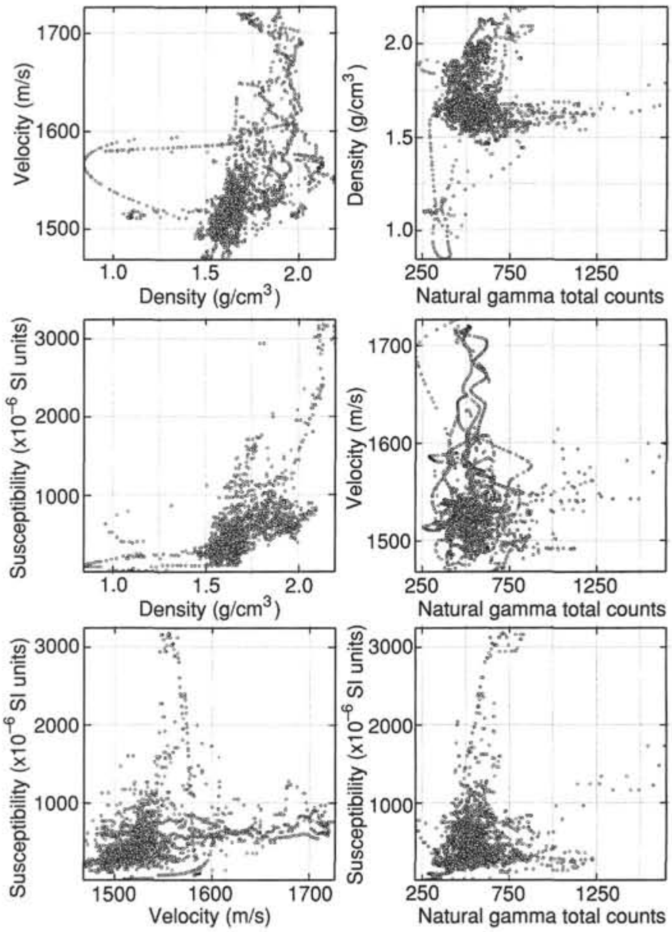

Figure 31. Two-dimensional crossplots of MST data, Hole 954A.

ods are presented in Table 11. Figure 41 presents the wet-water content and the porosity calculated using Method C, and the bulk density calculated using Method B, alongside downhole velocity. From the mud line to the onset of the volcanic breccia zone at 408 mbsf (lithologic Unit IV), there is a gradual increase with depth in density values from 1.73 to 1.98 g/cm^3, and a corresponding decrease in water content (38.10% to 26.78%) and porosity (61.38% to 49.38%), with a few anomalies at approximately 80, 180, 220, and 350 mbsf, which correspond to highs in measured velocity in the same intervals. Lithologically these zones are volcanic lapilli at 80 and 180 mbsf, an interval containing a dark lithic silty sandstone at about 220 mbsf, and a dark gray volcanic calcareous sandstone at 350 mbsf. Below 408 mbsf, there is an abrupt change in physical properties where average values for density increase from 1.85 to 2.69 g/cm^3, wet-water content decreases from 32.79% to 10.26%, and porosity from 55.63% to 24.60%. Figure 42 shows wet-water content, as well as void ratio and grain density calculated using Method C, alongside strength (vane shear and penetrometer values plotted together). The wet-water content and void ratio show strikingly similar trends and appear to correlate inversely with grain density and strength.

SEDIMENT ACCUMULATION RATES

A sediment accumulation curve has been constructed for Site 954 (Fig. 43) based on 24 nannofossil, 9 planktonic foraminiferal, and 11 paleomagnetic age determinations, giving a total of 44 points (Table 12). All microfossil datum levels were identified in pelagic layers or in burrow infills of hemipelagic sediment. There are at least three probable hiatuses, which are probably slump related: the first is at ~80 mbsf in the lower Pleistocene to uppermost Pliocene (~1.06–1.95 Ma), the second is at ~235 mbsf in the lower Pliocene (~4.4–5.3 Ma), and the third is at ~373 mbsf in the upper Miocene (~8.8–9.4 Ma).

Sediment accumulation rates are reasonably well constrained by microfossil and paleomagnetic datums down to ~370 mbsf. From 370 to 407 mbsf rates are less well constrained. Despite this, there is evidence to suggest a slump disturbed section with a thin interval of older material between 398.26 and 405.71 mbsf (see "Biostratigraphy," this chapter). Below 408 mbsf no datum levels could be used for the sediment accumulation rates in the basaltic breccia of lithologic Unit IV.

Sediment Accumulation Rates

From 0 to 80 mbsf in the upper part of lithologic Unit I, the accumulation rate is ~75 m/m.y., which probably results from a high background pelagic sedimentation rate combined with input of volcaniclastic sediment from Pleistocene volcanism on Gran Canaria. Alternatively, this section may be thickened by slumping. A hiatus that appears to be caused by slumping is present at ~80 mbsf, spanning ~0.89 m.y., from 1.06 Ma to 1.95 Ma.

From 80 to 235 mbsf in the middle and lower parts of lithologic Unit I, Unit II, and the upper part of Unit III, the accumulation rate appears to be constant at ~59 m/m.y. The end of the Roque Nublo phase of volcanism on Gran Canaria occurs in this interval. A hiatus

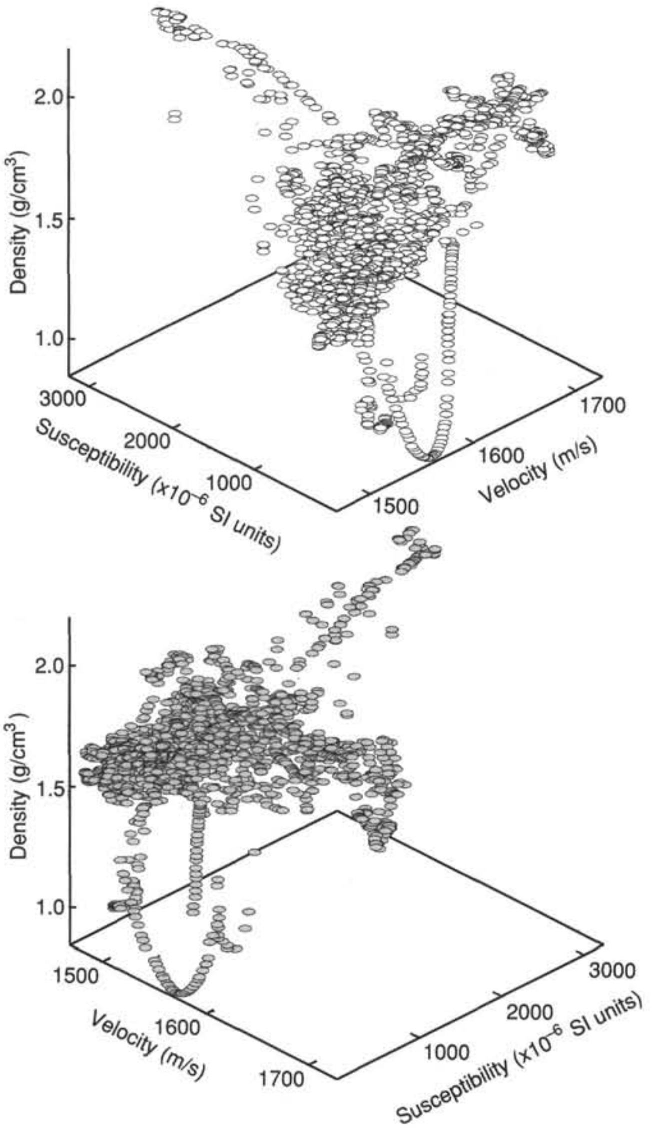

Figure 32. Three-dimensional crossplots of velocity, density, and magnetic susceptibility from MST data showing correlative trends, Hole 954A.

is present at 235 mbsf, spanning ~0.9 m.y., from 4.4 to 5.3 Ma. Again, this hiatus appears slump related. The beginning of Roque Nublo volcanism occurs during the span of this hiatus.

From 235 to 370 mbsf in lithologic Unit III, the accumulation rate is ~40 m/m.y. This rate appears to be well constrained by microfossil and paleomagnetic datums. Slumping is observed in this interval (see "Lithostratigraphy," this chapter), which corresponds to a hiatus in volcanic activity on Gran Canaria. At 370 mbsf, a hiatus appears to be present, spanning ~0.6 m.y., from 8.8 to 9.4 Ma. The end of the Fataga phase of volcanism on Gran Canaria occurred during the time span of this hiatus.

Material immediately below this hiatus is poorly constrained by two nannofossil datums and a single paleomagnetic datum and is difficult to interpret. Another hiatus may be present at ~398.26 mbsf, as there is a thin interval from 398.26 to 405.71 mbsf, which seems to belong to nannofossil Zone CN5 and which is anomalously old at more than 10.7 Ma. Below this interval, nannofossil Zone CN7 appears to be present again at 407.83 and Zones CN6 or 7 at 407.96 mbsf. Several possible explanations for this anomalously old section are discussed in the "Biostratigraphy" section, this chapter.

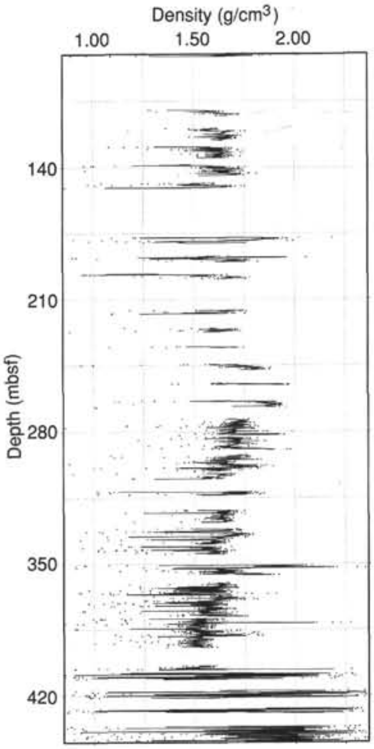

Figure 33. MST density, Hole 954B. Filtered data indicated by lines, raw data by discrete points.

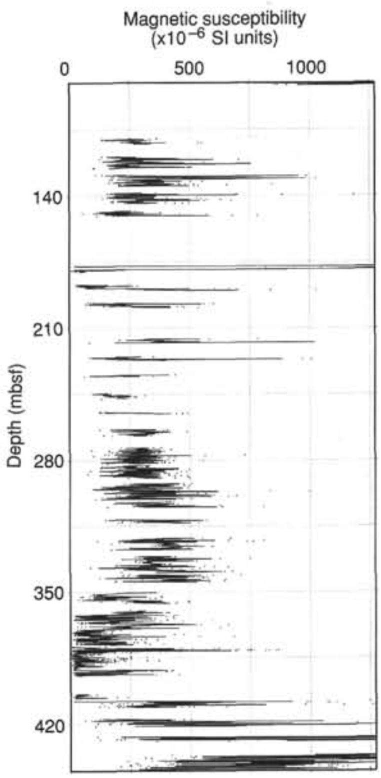

Figure 34. MST magnetic susceptibility, Hole 954B. Filtered data indicated by lines, raw data by discrete points.

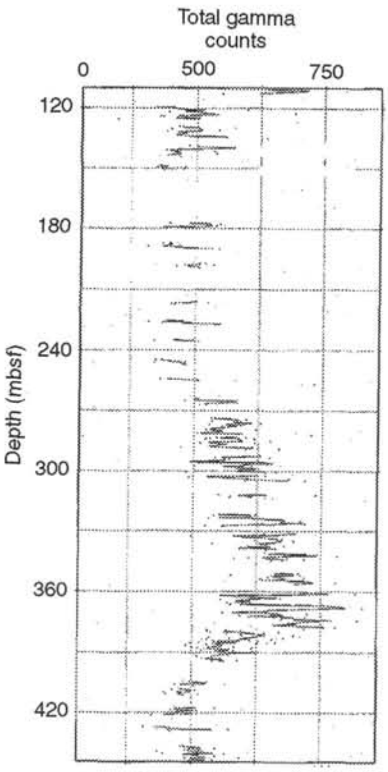

Figure 35. MST total natural gamma ray, Hole 954B. Filtered data indicated by lines, raw data by discrete points.

Below 408 mbsf, in the basaltic breccias of lithologic Unit IV, no microfossil or paleomagnetic datums could be determined, so the accumulation rate is unknown. Comparison with Site 953 where some datums were obtained in similar lithologies would suggest a minimum rate of ~70 m/m.y., with the real rate probably being somewhat higher.

IN-SITU TEMPERATURE MEASUREMENTS

Two ADARA temperature measurements were made using tool 12 at 39.0 and 67.5 mbsf while coring 157-954A-5H and 157-954A-8H. The mud line temperature was estimated at 2.819°C. Sub-bottom equilibrium temperatures were extrapolated from synthetic curves that were constructed to fit transient temperature data. These values were estimated at 5.712°C at 39.0 mbsf (Fig. 44) and 6.284°C at 67.5 mbsf (Fig. 45).

A geothermal gradient can be calculated from temperature measurements downhole; along with an estimate of thermal conductivity, the calculated gradient provides an estimate of heat flow. By plotting the sub-bottom equilibrium temperatures with the mud line temperature against depth, the geothermal gradient was approximated at 52.69°C/km by using a linear mean (Fig. 46). Heat flow was then calculated by multiplying the geothermal gradient by the average thermal conductivity for the hole (see "Physical Properties," this chapter). Thermal conductivity downhole at Hole 954A had an average value of approximately 1.0 W/(m·K), resulting in a heat flow value of 52.69 mW/m^2.

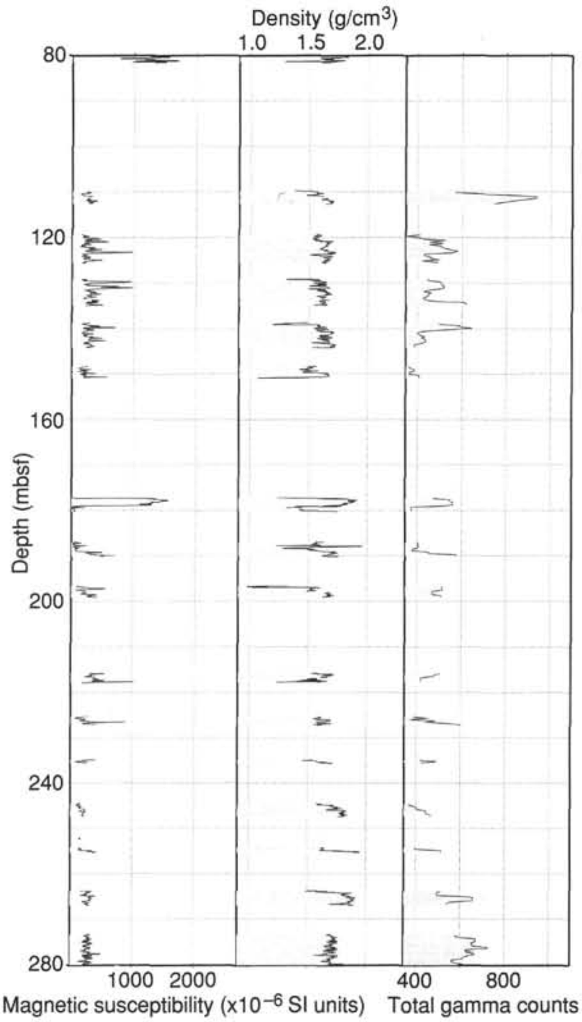

Figure 36. Filtered MST density, magnetic susceptibility, and natural gamma for 80–280 mbsf, Hole 954A.

REFERENCES

Gartner, S., 1992. Miocene nannofossil chronology in the North Atlantic, DSDP Site 608. *Mar. Micropaleontol.,* 18:307–331.

Rio, D., Fornaciari, E., and Raffi, I., 1990. Late Oligocene through early Pleistocene calcareous nannofossils from western equatorial Indian Ocean (Leg 115). *In* Duncan, R.A., Backman, J., Peterson, L.C., et al., *Proc. ODP, Sci. Results,* 115: College Station, TX (Ocean Drilling Program), 175–235.

Schmincke, H.-U., 1982. Volcanic and chemical evolution of the Canary Islands. *In* von Rad, U., Hinz, K., Sarnthein, M., and Seibold, E. (Eds.), *Geology of the Northwest African Continental Margin:* Berlin (Springer), 273–306.

————, 1994. *Geological Field Guide: Gran Canaria* (7th ed.): Kiel, Germany (Pluto Press).

Young, J.R., 1990. Size variation of Neogene *Reticulofenestra* coccoliths from Indian Ocean DSDP cores. *J. Micropaleontol.,* 9:71–85.

Young, J.R., Flores, J.-A., and Wei, W., 1994. A summary chart of Neogene nannofossil magnetobiostratigraphy. *J. Nannoplankton Res.,* 16:21–27.

Ms 157IR-108

NOTE: For all sites drilled, core-description forms ("barrel sheets") and core photographs can be found in Section 6, beginning on page 561. Smear-slide and thin-section data are given in Section 7, beginning on page 835. The CD-ROM (back pocket, this volume) contains physical properties and geochemical data, MST data, logging data, and color core photographs (Sites 950 and 953 only).

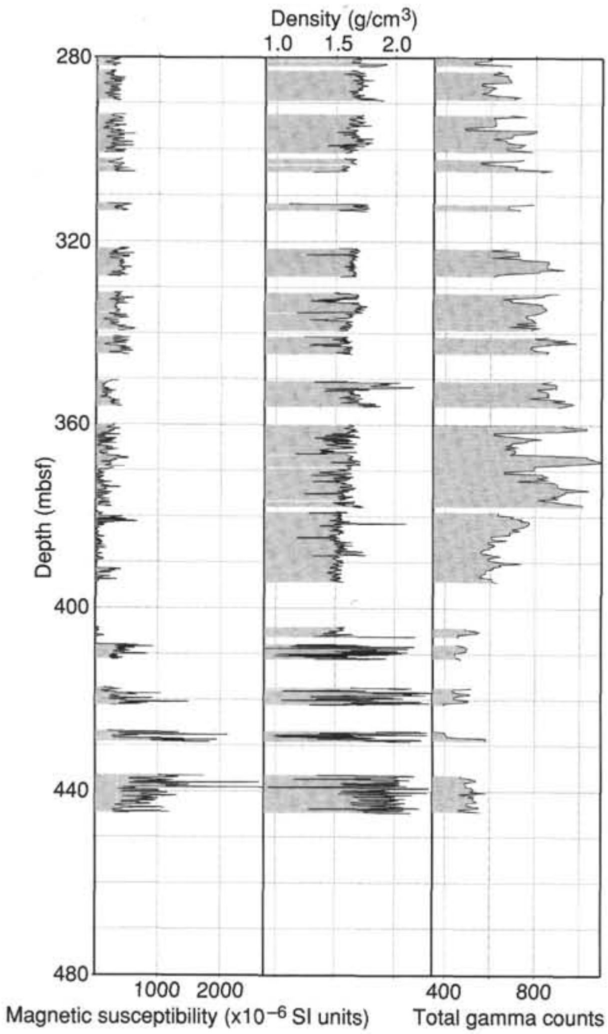

Figure 37. Filtered MST density, magnetic susceptibility, and natural gamma for 280–445 mbsf, Hole 954B.

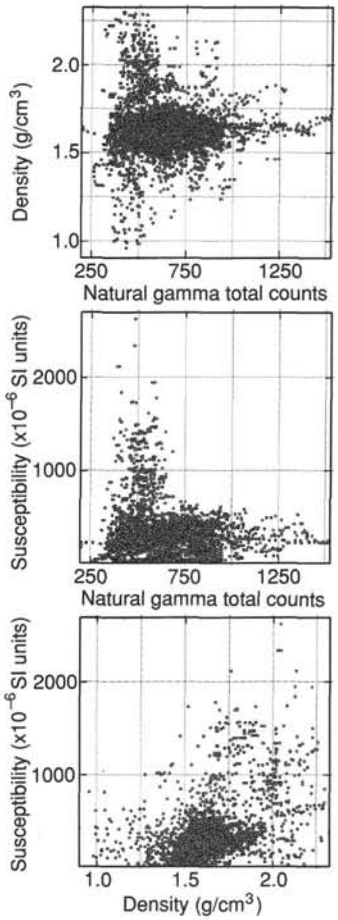

Figure 38. Two-dimensional crossplots of MST data, Hole 954B.

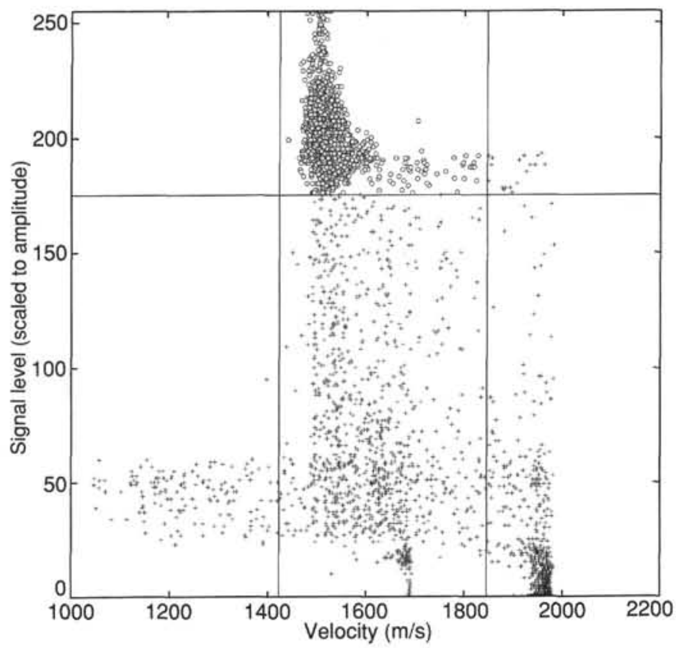

Figure 39. Example of data windowing for Hole 954A velocity. Filled circles represent accepted measurements. Excluded measurements are indicated by crosses.

Table 8. Thermal conductivity measurements, Hole 954A.

Core, section, interval (cm)	Depth (mbsf)	Method	TCcorr (W/mK)	Standard error (W/mK)	Drift (°/min)
157-954A-					
1H-1, 50	0.50	F	0.950	0.00504	–0.024
1H-3, 50	3.50	F	0.880	0.01636	–0.033
3H-1, 50	11.00	F	0.993	0.01314	0.000
3H-5, 50	17.00	F	0.977	0.01348	–0.035
4H-1, 50	20.50	F	0.967	0.00955	0.019
4H-5, 50	26.50	F	0.937	0.01015	–0.032
5H-1, 50	30.00	F	1.123	0.01106	0.016
5H-3, 50	33.00	F	0.992	0.01101	0.014
6H-1, 50	39.50	F	1.019	0.01013	–0.039
6H-3, 50	42.50	F	0.939	0.01424	0.005
6H-5, 50	45.50	F	1.158	0.01278	0.022
7H-1, 50	49.00	F	1.012	0.01430	0.032
7H-3, 50	52.00	F	1.083	0.01512	–0.009
7H-5, 50	55.00	F	1.306	0.01164	0.001
8H-1, 50	58.50	F	1.001	0.01296	0.005
8H-3, 50	61.50	F	1.080	0.01028	–0.011
8H-5, 50	64.50	F	1.215	0.01116	–0.020
9H-1, 50	68.00	F	1.024	0.01686	0.012
9H-3, 50	71.00	F	1.190	0.01106	0.001
9H-5, 50	74.00	F	1.148	0.01127	0.005

Notes: Method used either F = full-space or H = half-space. TCcorr = thermal conductivity corrected for drift.

Table 9. Velocity measurements, Holes 954A and 954B.

Core, section, interval (cm)	Depth (mbsf)	Velocity (km/s)	Tool	Temperature (°C)
157-954A-				
1H-1, 47–49	0.47	1.51	DSV	20.3
3H-1, 74–76	11.24	1.54	DSV	21.3
3H-2, 67–69	12.67	1.54	DSV	21.1
4H-2, 109–111	22.59	1.53	DSV	20.4
4H-4, 97–99	25.47	1.55	DSV	20.2
4H-7, 11–13	29.11	1.53	DSV	21.6
6H-2, 60–62	41.10	1.55	DSV	20.3
7H-1, 111–113	49.61	1.56	DSV	20.9
7H-2, 62–64	50.62	1.56	DSV	21.0
8H-1, 140–142	59.40	1.63	Ham	
8H-2, 128–130	60.78	1.64	Ham	
8H-3, 131–133	62.31	1.52	Ham	
8H-4, 87–89	63.37	1.58	Ham	
8H-4, 138–140	63.88	1.56	Ham	
8H-5, 43–45	64.43	1.63	Ham	
8H-6, 46–48	65.96	1.60	Ham	
8H-7, 36–38	67.36	1.55	Ham	
9H-1, 112–114	68.62	1.59	Ham	
9H-2, 124–126	70.24	1.59	Ham	21.4
9H-3, 146–148	71.96	1.53	Ham	21.0

Notes: Temperature = temperature of the sample. Tools are DSV or Hamilton Frame.

Only a part of this table is reproduced here. The entire table appears on the CD-ROM (back pocket).

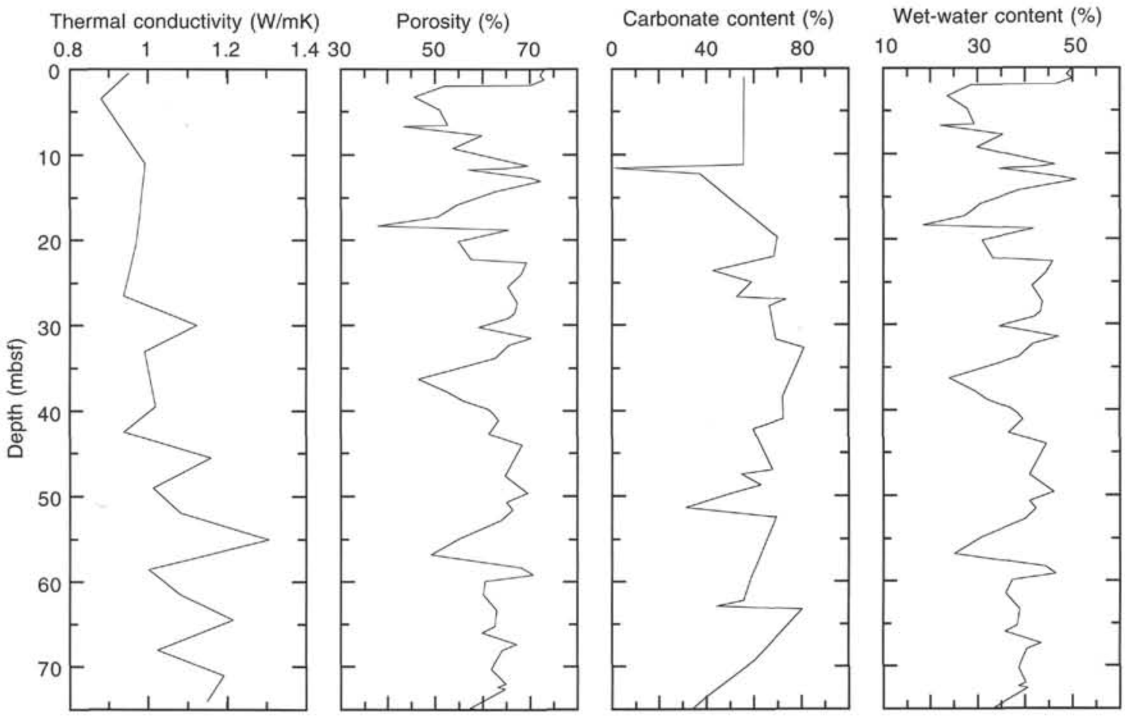

Figure 40. Thermal conductivity, porosity (Method C), carbonate content, and wet-water content, Hole 954A.

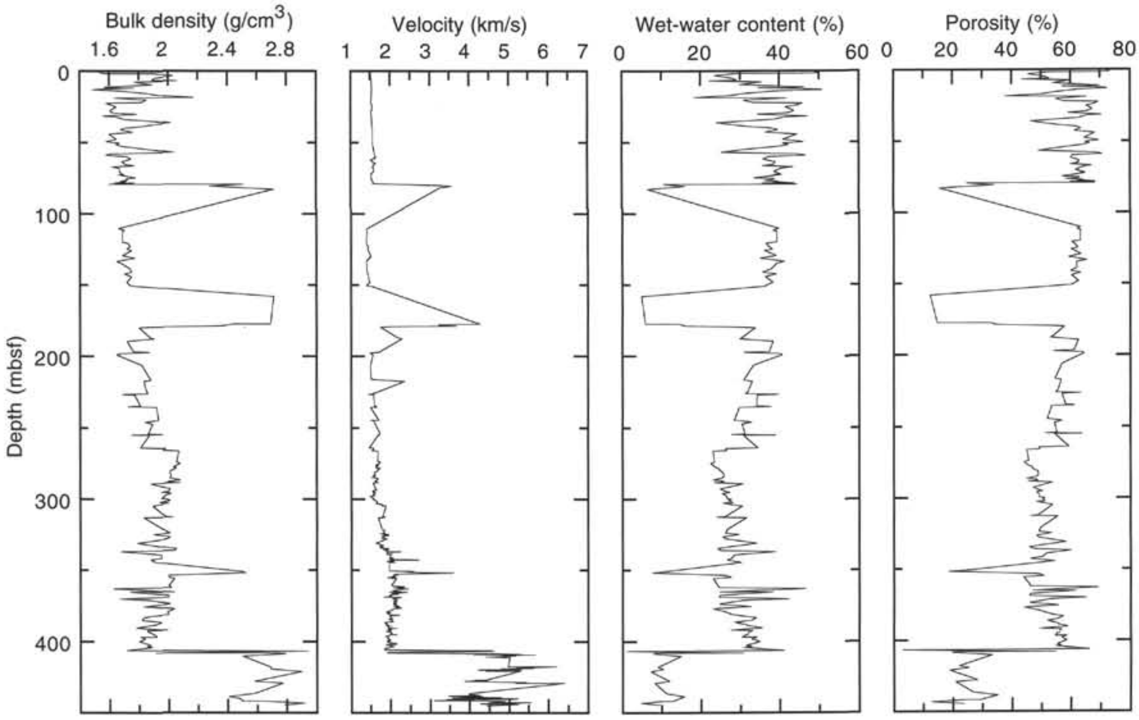

Figure 41. Bulk density (Method B), velocity, wet-water content, and porosity (Method C), Holes 954A and 954B.

Table 10. Strength measurements, Holes 954A and 954B.

Core, section, interval (cm)	Depth (mbsf)	Pk str (kPa)	Res (kPa)	Pe (kPa)
157-954A-				
1H-1, 50–51	0.50	5.20	2.0	
3H-1, 77–78	11.27	14.60	5.0	
3H-2, 70–71	12.70	29.80	19.1	
4H-2, 90–91	22.40			34.32
4H-2, 118–119	22.68			36.78
4H-3, 20–21	23.20			61.29
4H-3, 60–61	23.60			49.03
4H-3, 100–101	24.00			58.84
4H-4, 30–31	24.80			171.62
4H-4, 70–71	25.20			98.07
4H-4, 130–131	25.80			122.58
4H-5, 20–21	26.20			68.65
4H-5, 112–113	27.12	18.92	7.9	
4H-5, 120–121	27.20			78.45
4H-5, 131–132	27.31	30.70	17.6	
4H-6, 30–31	27.80			34.32
4H-6, 80–81	28.30			36.78
4H-6, 130–131	28.80			44.13
4H-7, 14–15	29.14	15.40	9.0	
5H-1, 22–23	29.72			49.03

Notes: Pk str = peak strength, undrained shear strength as measured by the vane shear, Res = residual shear strength, and Pen = unconfined shear strength as measured by the penetrometer, converted to kPa.

Only a part of this table is reproduced here. The entire table appears on the CD-ROM (back pocket).

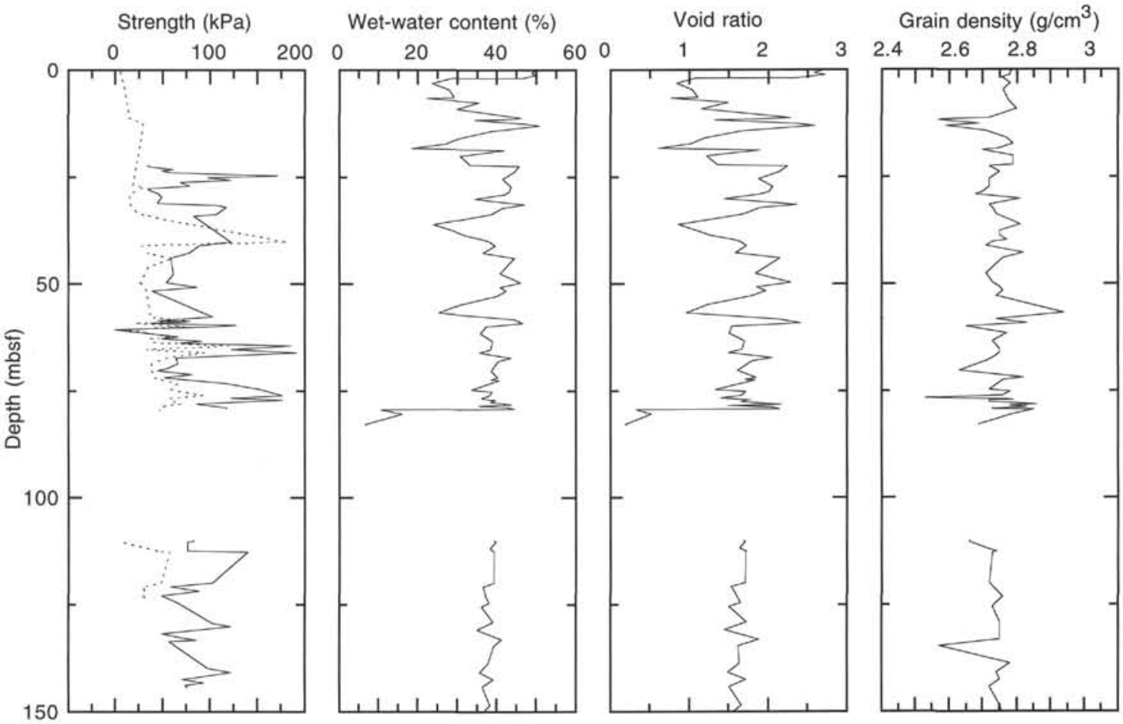

Figure 42. Vane shear (dashed line) and penetrometer (solid line) strength, wet-water content, void ratio (Method C), and grain density (Method C), Holes 954A and 954B.

Table 11. Index properties, Holes 954A and 954B.

Core, section, interval (cm)	Depth (mbsf)	WCw (%)	WCd (%)	BDb (g/cm^3)	BDc (g/cm^3)	GDb (g/cm^3)	GDc (g/cm^3)	DDb (g/cm^3)	DDc (g/cm^3)	Porb (%)	Porc (%)	VRb	VRc
157-954A-													
1H-1, 1–3	0.01	49.96	99.86	1.53	1.50	3.01	2.79	0.77	0.75	74.57	73.10	2.93	2.72
1H-1, 49–51	0.49	49.22	96.93	1.54	1.51	2.98	2.78	0.78	0.77	73.81	72.43	2.82	2.63
1H-1, 75–77	0.75	48.82	95.40	1.54	1.51	2.97	2.78	0.79	0.77	73.41	72.16	2.76	2.59
2H-1, 20–22	1.20	50.02	100.06	1.54	1.50	3.14	2.78	0.77	0.75	75.40	73.08	3.07	2.72
2H-1, 89–91	1.89	46.65	87.45	1.58	1.54	3.02	2.75	0.84	0.82	72.08	70.13	2.58	2.35
2H-1, 95–97	1.95	28.69	40.24	1.90	1.86	2.89	2.76	1.35	1.32	53.18	52.02	1.14	1.08
2H-2, 71–73	3.21	23.61	30.91	2.03	1.98	2.92	2.78	1.55	1.51	46.87	45.62	0.88	0.84
2H-3, 76–78	4.76	27.85	38.60	1.91	1.87	2.87	2.76	1.38	1.35	51.91	50.95	1.08	1.04
2H-4, 104–106	6.54	29.22	41.29	1.89	1.85	2.91	2.77	1.34	1.31	53.97	52.71	1.17	1.11
2H-4, 118–120	6.68	22.12	28.40	2.06	2.01	2.89	2.77	1.60	1.57	44.45	43.46	0.80	0.77
2H-5, 76–78	7.76	35.43	54.88	1.77	1.73	2.94	2.78	1.14	1.12	61.15	59.83	1.57	1.49
2H-6, 76–78	9.26	29.85	42.56	1.89	1.85	2.95	2.80	1.33	1.29	55.07	53.79	1.23	1.16
3H-1, 76–78	11.26	46.30	86.22	1.57	1.54	2.89	2.72	0.84	0.83	70.89	69.63	2.43	2.29
3H-1, 109–111	11.59	42.12	72.78	1.62	1.57	2.81	2.58	0.94	0.91	66.65	64.71	2.00	1.83
3H-1, 122–124	11.72	34.61	52.92	1.77	1.69	2.86	2.57	1.15	1.10	59.66	56.99	1.48	1.33
3H-2, 69–71	12.69	47.46	90.31	1.55	1.52	2.92	2.69	0.82	0.80	72.01	70.35	2.57	2.37
3H-2, 106–108	13.06	50.76	103.09	1.49	1.46	2.79	2.59	0.73	0.72	73.74	72.24	2.81	2.60
3H-3, 75–77	14.25	38.84	63.50	1.69	1.65	2.90	2.71	1.04	1.01	64.22	62.71	1.79	1.68
3H-4, 87–89	15.87	30.71	44.31	1.86	1.82	2.91	2.77	1.29	1.26	55.71	54.51	1.26	1.20
3H-5, 75–77	17.25	27.16	37.28	1.94	1.90	2.91	2.79	1.41	1.39	51.44	50.41	1.06	1.02

Notes: WCw = water content (% wet sample weight), WCd = water content (% dry sample weight), BD = bulk density, GD = grain density, DD = dry density, Por = porosity, and VR = void ratio. Suffixes "b" and "c" on column heads indicate value calculated using Method B and Method C, respectively (see "Explanatory Notes," this volume).

Only a part of this table is reproduced here. The entire table appears on the CD-ROM (back pocket).

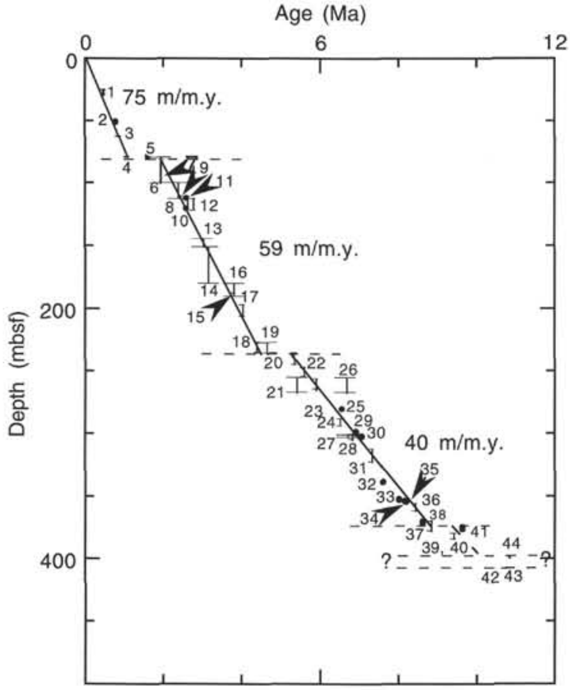

Figure 43. Sediment accumulation rates for Hole 954A. Vertical bars represent distances between sample points. Numbers refer to datum levels given in Table 12.

Table 12. Datum levels used in calculation of sediment accumulation rate curves.

	Event	Sample Top	Sample Bottom	Depth (mbsf) Top	Depth (mbsf) Bottom	Age (Ma)
		157-954A-	157-954A-			
1	LO *P. lacunosa*	4H-4, 60	4H-7, 8	25.10	29.08	0.46
2	C1n (o)/Brunhes-Matuyama	7H-2, 55	7H-2, 105	50.50	51.00	0.78
3	LO *R. asanoi*	8H-3, 120	8H-4, 35	62.20	62.85	0.83
4	FO *R. asanoi*	10H-2, 12	11X-CC, 14	78.62	79.34	1.06
5	LO *C. macintyrei*	11X-CC, 14	1R-1, 122	79.34	81.42	1.60
6	FO *Gr. truncatulinoides*	11X-1, 0–2	3R-CC, 0–2	79.22	100.11	1.92
		157-954B-	157-954B-			
7	LO *D. brouweri*	1R-1, 122	3R-CC, 0	81.42	100.10	1.95
8	LO *Gr. miocenica*	3R-CC, 0–2	4R-CC, 0–2	100.11	112.69	2.37
9	LO *D. pentaradiatus*	3R-CC, 0	4R-1, 69	100.10	110.39	2.44
10	C2An (t)/Gauss (t)	4R-2, 110	5R-1, 0	112.00	120.00	2.60
11	LO *D. surculus*	4R-1, 69	4R-2, 105	110.39	112.25	2.61
12	LO *D. tamalis*	4R-CC	5R-2, 89	112.68	121.69	2.76
13	LO *Gr. multicamerata*	7R-CC, 0–2	8R-CC, 0–2	144.20	150.92	3.00
	LO *Gq. altispira*					3.09
14	LO *Ss. seminulina*	8R-CC, 0–2	11R-CC, 0–2	150.92	180.28	3.15
15	LO *R. pseudoumbilicus*	12R-1, 89.5	12R-CC	187.80	190.18	3.77
16	LO *Gr. margaritae*	11R-CC, 0–2	12R-CC, 0–2	180.28	190.19	3.79
17	FO *D. tamalis*	13R-1, 71	14R-CC, 5.5	197.21	206.26	4.01
18	LO *Amaurolithus* spp.	16R-2, 40	17R-1, 16	227.10	234.96	4.39
19	LO *Gg. nepenthes*	16R-CC, 0–2	17R-CC, 0–2	227.25	235.71	4.63
20	LO *Tq. rugosus*	17R-1, 58	18R-1, 33–34	235.38	244.73	5.34
21	LO *Gr. conomiozea* and *Gr. juanai*	19R-CC, 0–2	20R-CC, 0–2	255.39	267.09	5.40
22	LO *D. quinqueramus*	18R-CC	19R-1, 4	247.40	254.14	5.56
23	LO *A. amplificus*	19R-CC, 71	20R-1, 95	256.09	264.65	5.88
24	FO *A. amplificus*	22R-4, 62	23R-1, 112	287.92	293.52	6.50
25	C3A.n2 (o)	21R-5, 65	21R-5, 115	280.00	280.50	6.56
26	FO *Gr. margaritae*	19R-CC, 0–2	20R-CC, 0–2	255.39	267.09	6.64
27	FO *Gr. conomiozea*	23R-CC, 0–2	24R-1, 96–97	300.87	302.96	6.70
28	FO *R. pseudoumbilicus*	23R-6, 26	24R-2, 88	300.16	304.36	6.80
29	C3Bn (t)	23R-5, 25	23R-5, 75	298.50	299.50	6.92
30	C3Bn (o)	24R-1, 15	24R-1, 55	302.00	303.00	7.07
31	FO *A. primus*	25R-1, 48	26R-1, 78	312.18	322.18	7.30
32	C4n.2n (t)	27R-5, 85	27R-5, 125	338.00	339.00	7.62
33	C4n.2n (o)	29R-2, 25	29R-2, 55	352.00	353.00	8.03
34	C4r.1n (t)	29R-3, 15	29R-3, 65	353.50	354.00	8.17
35	C4r.1n (o)	29R-4, 10	29R-4, 45	354.50	355.00	8.21
36	FO *D. quinqueramus/berggrenii*	29R-4, 96	30R-2, 26	355.35	361.57	8.40
37	C4An (t)	31R-1, 65	31R-2, 15	370.00	371.50	8.63
38	LO *R. pseudoumbilicus*	31R-1, 70	31R-6, 118.5	370.10	377.83	8.80
39	FO *M. convallis*	32R-1, 93	32R-4, 105	379.83	384.26	9.40
40	LO *D. hamatus*	32R-1, 93	32R-4, 105	379.83	384.26	9.40
41	C5n.1n (t)	31R-4, 65	31R-5, 105	374.50	376.50	9.64
42	FO *D. hamatus*	35R-1, 3	35R-1, 16	407.83	407.96	10.40
43	FO *C. coalitus*	35R-1, 16	35R-1, 46	407.96	408.26	10.70
44	LO *C. miopelagicus*	33R-CC, 6	34R-1, 16	398.07	398.26	10.80

Notes: Numbers in left column refer to numbers on Figure 43.

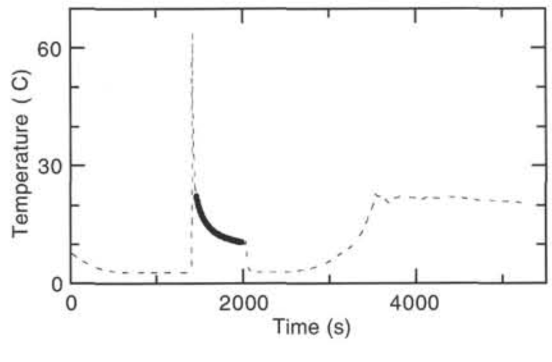

Figure 44. Measured temperatures (ADARA Tool 12) starting from the approximated zero time at the mud line and continuing through to the extraction of Core 157-954A-5H, 39.0 mbsf. The equilibrium temperature was extrapolated as 5.712°C. Dashed line shows measured temperature; solid line shows calculated temperature.

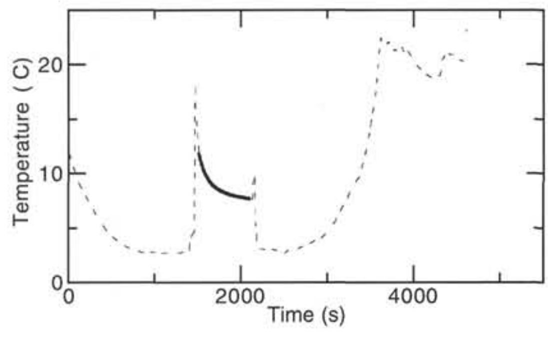

Figure 45. Measured temperatures (ADARA Tool 12) starting from the approximated zero time at the mud line and continuing through to the extraction of Core 157-954A-8H, 67.5 mbsf. The equilibrium temperature was extrapolated as 6.284°C. Dashed line shows measured temperature; solid line shows calculated temperature.

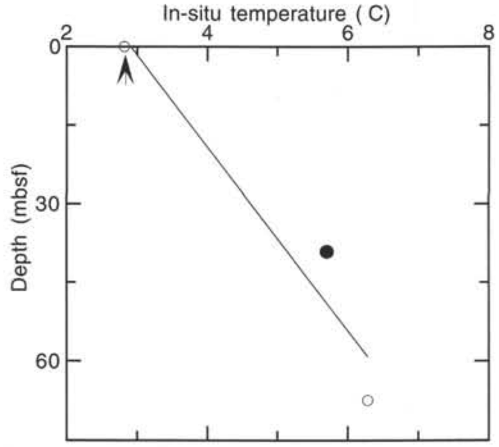

Figure 46. Hole 954A geothermal gradient from in-situ temperature measurements. The mud line (2.819°C, indicated by arrow) and equilibrium temperatures plotted vs. depth; the slope gives the geothermal gradient at 52.69°C/km ($y = 3.06779 + 0.05269x$). Filled circle = Core 157-954A-5H, 39.0 mbsf, 5.712°C; open circle = Core 157-954A-8H, 67.5 mbsf, 6.284°C.